

Department of Physics and Astronomy
Heidelberg University

Master thesis in Physics

submitted by

Vivienne Leidel

born in Heidelberg

2023

**From Cooling Atoms
Towards a Two Dimensional Fermi Gas**

This Master thesis has been carried out by

Vivienne Leidel

at the

Physikalisches Institut Heidelberg

under the supervision of

Prof. Dr. Selim Jochim

From cooling atoms towards a two dimensional fermi gas:

Heidelberg Quantum Architecture is a new experiment using ultracold Lithium-6 atoms aiming to achieve rapid cycle times of well under one second. Among others, the approach is to speed up the MOT loading with more available laser power enabling the use of a high flux 2D MOT as the cold atom beam source. All optical setups are built in a modular fashion with micrometer reproducibility.

In particular setting up a laser lock to the Lithium-6 D2 transition using a modulation transfer scheme to ensure minimal drifts in frequency will be presented. An AOM doublepass module enabling high stability and quick setup times is presented.

Physics in lower dimension often exhibits peculiar properties. Hence, we want to fine tune the dimensionality of the system using a miniaturized accordion lattice setup. It consists of two laser beams intersecting at a tunable angle. In this way controlling the spacing between the interference fringes, and therefore the strength of the confinement of our atom is possible.

Von Atomkühlung zu einem zweidimensionalen Fermi-Gas:

Heidelberg Quantum Architecture ist ein neues Experiment bei dem ultrakalte Lithium-6-Atome verwendet werden, um schnelle Zykluszeiten von unter einer Sekunde zu erreichen. Der Ansatz besteht unter anderem darin, die MOT-Laderate mit mehr Laserleistung zu beschleunigen, was eine Verwendung einer 2D-MOT ermöglicht. Die optischen Aubauten sind Reproduzierbarkeit im Mikrometerbereich, was durch ein modulares Design ermöglicht wird. Insbesondere wird die Einrichtung eines Laserlock für den Lithium-6-D2-Übergang unter Verwendung eines Modular-Transfer Signal vorgestellt, das minimale Frequenzabweichungen sicherstellt. Es wird ein AOM-Doppelpassmodul verwendet, das eine hohe Stabilität und schnelle Aufbauzeiten ermöglicht. Die Physik in niedrigeren Dimensionen weist oft besondere Eigenschaften auf. Daher wollen wir die Dimensionalität des Systems mit Hilfe eines miniaturisierten Akkordeongitters verändern. Es besteht aus zwei Laserstrahlen, die sich in einem einstellbaren Winkel kreuzen. Auf diese Weise können wir den Abstand zwischen den Interferenzstreifen und damit die Stärke des Einschlusses unserer Atome steuern.

CONTENTS

1	INTRODUCTION	1
2	HEIDELBERG QUANTUM ARCHITECTURE	5
2.1	Motivation	5
2.1.1	Lithium-6	5
2.1.2	Goals of the new experiment	6
2.2	Experimental setup	7
2.2.1	Vacuum	7
2.2.2	Mounting	8
I	ROAD TO 2D MOT/HOW TO GET FAST	11
3	LASERSYSTEM	13
3.1	Laser setup	13
3.1.1	TA-SHG	13
3.1.2	Characterization	15
3.2	Changing the frequency of the laser	17
3.3	Spectroscopy	18
3.4	Lock	18
3.4.1	DLCpro Lock	19
3.4.2	Red Pitaya Lock	19
3.4.3	Comparison	20
4	MAGNETO OPTICAL TRAP	23
4.1	Laser cooling and trapping	23
4.1.1	Laser cooling	23
4.1.2	Trapping	25
4.1.3	Cooling in ${}^6\text{Li}$	26
4.2	Setup Distribution	27
4.2.1	Doublepass	27
4.2.2	Distribution	29
4.2.3	Beat note	30
4.3	MOTs	31
4.3.1	2D-MOT	31
4.3.2	3D-MOT	33
II	ACCORDION LATTICE/PLANNING OF A MODULE	35
5	ACCORDION LATTICE	37
5.1	Theory and Simulations	38
5.2	Confinement	42
5.3	Overview of existing accordion lattices approaches	43
5.4	NPBS as way to go?	44
5.5	Beam translation	45
5.6	Parameters of the planned setup	47
5.7	Experimental setup	50
5.7.1	Alignment	50
5.7.2	Measurement	53
5.7.3	Stability	55

5.7.4	Limitations and choosing the right components	58
5.8	Towards a module	59
6	CONCLUSION AND OUTLOOK	63
III	APPENDIX	65

INTRODUCTION

"At finite temperatures continuous symmetries cannot be spontaneously broken in systems with sufficiently short-range interactions and dimension less or equal two."

- Mermin-Wagner theorem [1]

For several reasons low-dimensional systems are of particular interest, one of them being the Mermin-Wagner theorem. This very general theorem has a wide range of applications. Historically the first version of the theorem was about the possibility of ferromagnetic or antiferromagnetic order in one and two-dimensional systems [1]. Thus stating that no long-range order is possible at finite temperatures and therefore no ferromagnetic phase transition happening. Shortly after Hohenberg showed the theorem for bosonic- and fermionic-systems with regards to superconductivity and superfluidity [2] showing its applicability not only to classical systems but also quantum mechanic ones. Over the years various applications have been investigated from crystalline order in two-dimensions [3] to hydrodynamics [4]. While this shows that there are many instances where a restriction of dimensions can be of interest until this point it was only theoretical considerations.

To check the applicability to the real world, experiments are required. In our case this means a possibility to lower the dimension of our ultracold fermi gas is necessary. Here the challenge is to load a large fraction of an initial 3D gas into a trap with strong confinement along one axis and relative weak one along the other two, thus making it 2D. One practical solution is an accordion lattice, which allows to tune the confinement along the third direction.

The experimental realisation gives the opportunity to investigate a huge amount of different systems. Physical systems are fully determined by their Hamiltonian, as they contain all informations of the behaviour and time evolution of the system. Consequently, to investigate and simulate different systems, the capability to tune the parameters of the Hamiltonian is needed. Here the versatility of cold atoms gives the opportunity to do quantum simulations by enabling tuning and construction of Hamiltonians via optical potentials and magnetic fields. The Hamiltonian can be constructed starting from the spacial confinement of the atoms by optical potential, the interaction strength between the atoms can be tuned via a magnetic field due to the Feshbach resonance and the dimensionality by an accordion lattice. Apart from the Hamiltonian, the initial state needs to be prepared in a deterministic way. The atoms are prepared by loading and cooling them to one particular state. In our group there is a peculiar interest in performing few fermion experiments. Therefore a scheme to realize the transition from many particles to a predetermined small number of atoms is required. This is done via spilling [5]. Fermions populate, due to Pauli exclusion, each energy state in a harmonic potential, only with a deterministic, low number of particles. By applying a magnetic field gradient to the atoms trapped in a harmonic potential the trap walls are lowered and high energy atoms escape the trap, leaving a few-body fermionic system.

To gain information of the prepared system the results are imaged. For this task, a high-performance microscope objective is employed [6]. Single atom detection allows the observation of the behaviour of few particles at small scales. Further a spin resolved imaging scheme can be used to get correlations in momentum space [7].

For real world applicability some theoretical assumptions need to be modified. While this changes the system, it does not make lower dimensions less interesting, due to its still present rich interplay of thermal and quantum fluctuations. While the short-range interaction is nearly always fulfilled, the continuous symmetry is not. One example are most real magnets, due to their spin-orbit coupling of the electrons, an anisotropy is imposed which breaks the continuity of the symmetry. But even without fulfilling the assumption of a continuous symmetry, systems exhibit peculiar properties in lower dimensions. One example is the Ising model, which was first introduced in the 1920s to understand how the phase transition between paramagnetism and ferromagnetism occurs. Here the dimension of the physical problem is reduced, not for an explicit interest in lower dimensions but to make it theoretically solvable, as it was often done in the last centuries. Compared to previous systems, this model has a discrete symmetry. While an exact solution was found for the one [8] and two dimensional case [9], for three dimensions it was only solved using numerical simulations [10]. The one dimensional approach has no phase transitions but the two and three dimensional cases have and are as such able to capture the behaviour of real magnets. As such it differs from the Mermin-Wagner theorem but interesting phenomena take place.

In experiment the inexplicit assumption of free particle can not hold. Leading to finite size effects and results which differ from the theorem. This can for example be seen in graphene. Graphene consists of a single layer of carbon atoms arranged in a hexagonal lattice structure. Following Mermin Wagner it seems that the existence of systems, like graphene, are forbidden. If one plugs in the numbers for a graphene sheet at room temperature this long-range order is broken at a size of $l > 10^{30}\text{m}$ [11].

Although phase transition stemming from spontaneous symmetry breaking are impossible in lower dimensions, new phase transitions arise. A well-known topological phase transition in two dimensions is the Berezinskii-Kosterlitz-Thouless phase transition [12, 13] from a superfluid to a normal state. This allows for a quasi-long range order and the emergence of a quasi-condensate [14].

This and other phenomena have already been confirmed experimentally and relevant parameters such as the critical temperature have been determined.

But still many opportunities and theories await to be explored. For this purpose a new experiment [Heidelberg Quantum Architecture \(HQA\)](#) is built at Heidelberg University. A major goal of this experiment is to keep the experiment time as short as possible. With cycle time well below 1s, the number of cycles in a given time frame is drastically increased compared to current setups. Allowing for huge data amounts to be generated and for simulations to be finished faster. Optical setups are planned in a modular way, to lessen the time needed for adjustment and allowing a exchangeability of the components. This not only simplifies maintenance of the setup as real-time feedback from the atoms becomes reality, but also opens up a variety of new and complex systems to investigate.

This thesis gives insight in the current status of the [HQA](#) experiment with focus on the realization of the [Magneto Optical Traps \(MOTs\)](#) and the accordion lattice. In the second chapter a detailed overview of the experimental setup is given. Here the motivation and goals as well as the fundamental design ideas and their consequences for the further setup are described.

The third chapter describes the laser system, from the light source to the frequency locked output. This is done by locking the laser via [Proportional–Integral–Derivative Controllers \(PIDs\)](#) to an atomic transition given by a spectroscopy.

Chapter four gives insight into the implemented [MOTs](#), from the theoretical background via the laser distribution and frequency shifts to the 2D- and 3D-[MOT](#).

The last chapter is about the accordion lattice. An accordion lattice allows us to change the dimensionality of a system in a controlled way and therefore paves the way for a well controlled 2D system and the characterization of the influence of the 2D-ness on the atomic sample. Here a new approach with an [Nonpolarizing Beam Splitter \(NPBS\)](#) and a high NA objective is taken to miniaturize the module and increase stability as well as reproducibility.

There is already a vast amount of ultracold quantum gases experiments using various species of atoms. Even if we limit it to experiments using Lithium-6 there are still multiple groups working with it. So what is the reason for the wide use of Lithium-6? And what is to gain from a new setup? This will be addressed in the following chapter. Further a quick overview of the experiment implementation of Heidelberg Quantum Architecture will be shown, to give a context for the following work.

2.1 MOTIVATION

2.1.1 Lithium-6

Controlling neutral atoms with lasers is only possible if there is an interatomic electric transition available at the wavelength of an existing laser. Lithium along with all other alkalis, contains the noticeable spectroscopic D-line which can be used for laser cooling. Additionally, due to being an alkali metal, it has a single valence electron leading to a simple hydrogen like structure. There are two stable isotopes present namely ^7Li and ^6Li . While ^7Li is a boson due to its four neutrons and single valence electron, ^6Li is a fermion with three neutrons.

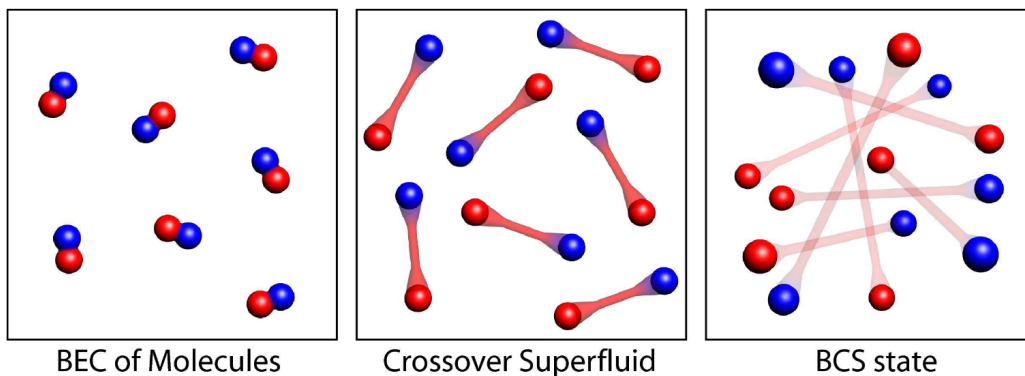


Figure 1: Crossover from BEC of molecules to a BCS state. By applying a magnetic field the interparticle distance is tuned from the formation of tightly bound molecules to the BCS-limit of long-ranged Cooper pairs, where the size of the pairs is much larger than the inter-particle spacing. On resonance, one enters the unitarity regime where the pair size is on the same order as the inter-particle spacing. The picture is taken from [15].

Bosons follow the Bose-Einstein statistic and bunch together. This gives for low temperatures rise to a macroscopic quantum phenomenon called the Bose-Einstein Condensation (BEC). Fermions on the other hand behave antibunching and follow the Fermi-Dirac statistic. Instead of a BEC they form a Fermi sea, an incompressible sea of particles. By adding arbitrary weak attractive interactions to a filled

Fermi sea, bound states are forming. These so called Cooper pairs are for example a fundamental ingredient for superconductivity.

Ideally one would want to investigate both phenomena with a single atomic species. This is possible with fermionic ${}^6\text{Li}$. Thanks to the presence of a Feshbach resonance, the scattering length can be tuned via a magnetic field allowing to form molecules. Molecules consisting of two half-integer fermionic particles behave like a boson. Thus with the help of the Feshbach resonance a crossover between the BEC and BCS regime is achieved.

2.1.2 Goals of the new experiment

Using the experience and knowledge gained from existing lithium-6 experiments, **HQA** pursues the goal of a modular design and fast cycle times, with the idea in mind of overcoming the limitations of existing setups. Examples being the amount of data that can be taken in a fixed time frame, the control of magnetic field curvatures or a fast thermalization into optical tweezer. One limitation of the cycle time for example being the **MOT** loading rate achieving cycle times within a few seconds. A considerable amount of time is used on the **3D-MOT** loading with it alone being on the order of a few seconds. Therefore it is necessary to rethink this process (see chapter 4). Higher cycle rates open up the opportunity to generate higher amounts of data, in the same time frame allowing to investigate for example high order correlation. Furthermore, it allows for easy debugging of the experiment, regular recalibration leading to increased fidelities and the implementation of machine learning.

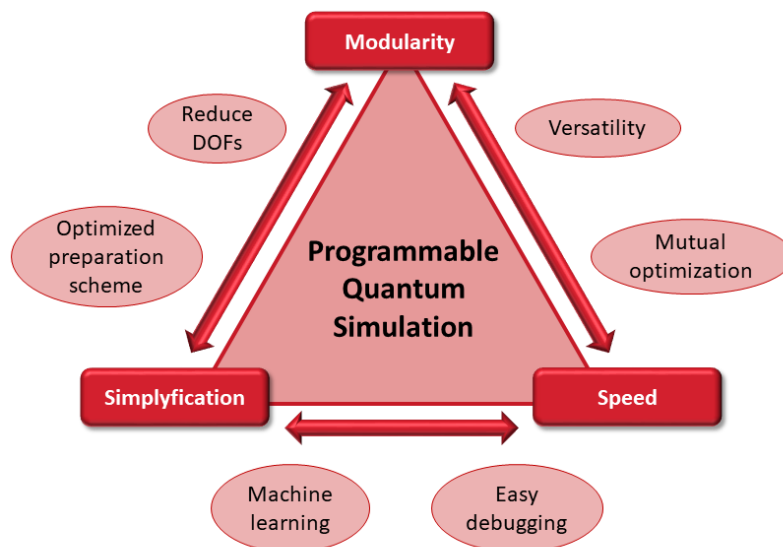


Figure 2: Overview of the conceptual ideas of **HQA**. The main aspects which are also highlighted in this thesis are visible in the corners of the triangular. In between their common points are presented.

Another limiting factor is the presence of a steel scientific chamber. Due to steel being conductive, Eddy currents limit the rate at which magnetic fields as well as screening RF and microwave fields can change, thus a glass cell is used instead. To

prevent contamination of the glass cell window due to lithium-6 atoms, a 2D-MOT is installed instead of a Zeeman slower. Since a Zeeman slower needs the oven to be in direct line of sight of the 3D-MOT position, the atoms then have a direct path to the glass cell window, leading to coating of said window by untrapped ${}^6\text{Li}$. Additionally to ensure that future developments are not limited by decisions made now, the setup is planned modular whenever possible. It means that planned setups are simplified i.e. reduce unwanted degrees of freedom, use stable solutions and have a universal interface to be exchangeable between ports, but also and maybe more important, between experiments. This allows the modules to be exchangeable and adaptable. To realize this, the setup needs to be build in such a way that a module can be placed at various positions, since the laser beam has the same height and position with respect to the hole row over the entire breadboard. Moreover a modular approach allows to put modules out of the setup allowing to characterize components outside of the setup giving access to a variety of new characterization possibilities and making debugging of the experiment easier. Examples for such modules can be found in 4.2.1 and 5.8.

2.2 EXPERIMENTAL SETUP

2.2.1 *Vacuum*

The whole preparation of the ${}^6\text{Li}$ -atoms happens in a vacuum chamber. The apparatus can be seen in figure 3, including the oven, the ion pumps, the 2D-MOT and the glass cell. Ultra high vacuum is required to avoid collisions with stray particles such that the sample can be prepared deterministically. The lithium used for the experiments is stored in an oven located directly beneath the 2D-MOT. Here approximately 9g ${}^6\text{Li}$ and 0.1g ${}^7\text{Li}$ are stored. This amount should be enough for several years of experiments.

With heating wires around the oven the temperature can be regulated. Around 350 °C, lithium atoms leave the oven after evaporation towards the 2D-MOT. The 2D-MOT is situated above the oven, the laser beam going in a bowtie configuration is made visible in red in figure 3. The red beam coming from the left is a push beam to improve the transfer from the 2D- to 3D-MOT. Around the glass cell the 3D-MOT is built. Details and realization of the MOTs are described in chapter 4. The octagonally shaped glass cell is mounted to the vacuum via a glass to metal transition to match the thermal expansion coefficients of the glass cell and the steel flange. To do experiments seven side windows 0.5" and two vertical windows 1.5" are present. They are coated with a special nanostructure on the in- and outside allowing incident angles over 50° and reflectivities below 1%. The coating further allows a wide range of wavelength, from UV light at 400 nm up to IR light above 1.5 μm [16].

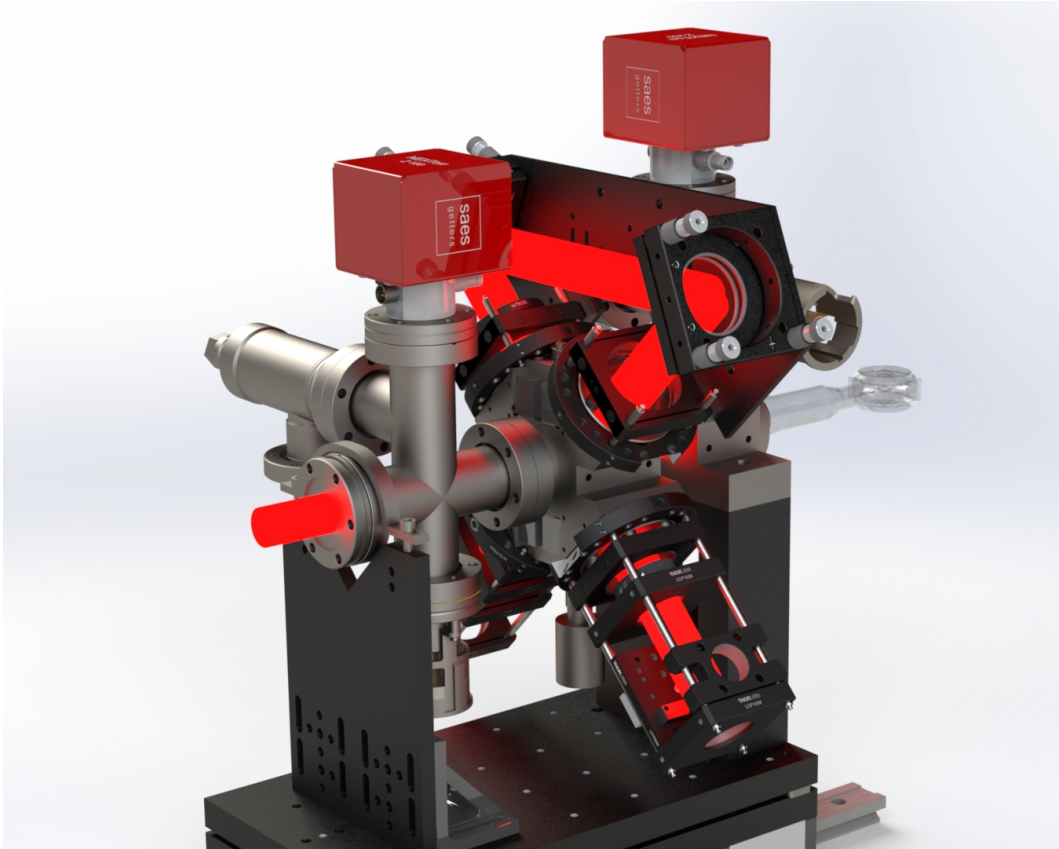


Figure 3: Rendering of the vacuum setup. In red the laser beams are visualized. On top of the vacuum chamber two ion pumps (red) maintain the vacuum pressure. In between the 2D-MOT chamber is situated. On the right the glass cell can be seen.

2.2.2 Mounting

The whole vacuum chamber is lifted up and placed on a rail system allowing to move the glass cell in and out of the magnetic field coils and the surrounding optics. This allows to measure the magnetic field at the position of the atoms as well as characterization of optical potentials. To ensure that after sliding the chamber in and out, the glass cell is situated at the same position, a fixed stop is mounted between the rails. The elevation of the rails allows for an optical path below and more space in between the breadboard and the table on the right.

For the optics around the glass cell a single breadboard is designated for each side viewport. The breadboard design and placement follows the octagonal structure of the glass cell as is shown in figure 4. It is intended to use these breadboards for the modules. They can be slid in along carvings in the breadboardplate. This allows to place the modules with a precision of a few μm by using dowel pins.

The coils are mounted around the glass cell and kept in place with titanium rods fixed to the upper and lower breadboard. The current and water supply cables are going outwards by bending them into the deeper craving on the right side. Thus allowing for additional parts to be mounted above.

Directly below the glass cell the imaging objective is mounted with a precision of $10\mu\text{m}$ [6]. This position is fixed and everything is mounted with respect to it.

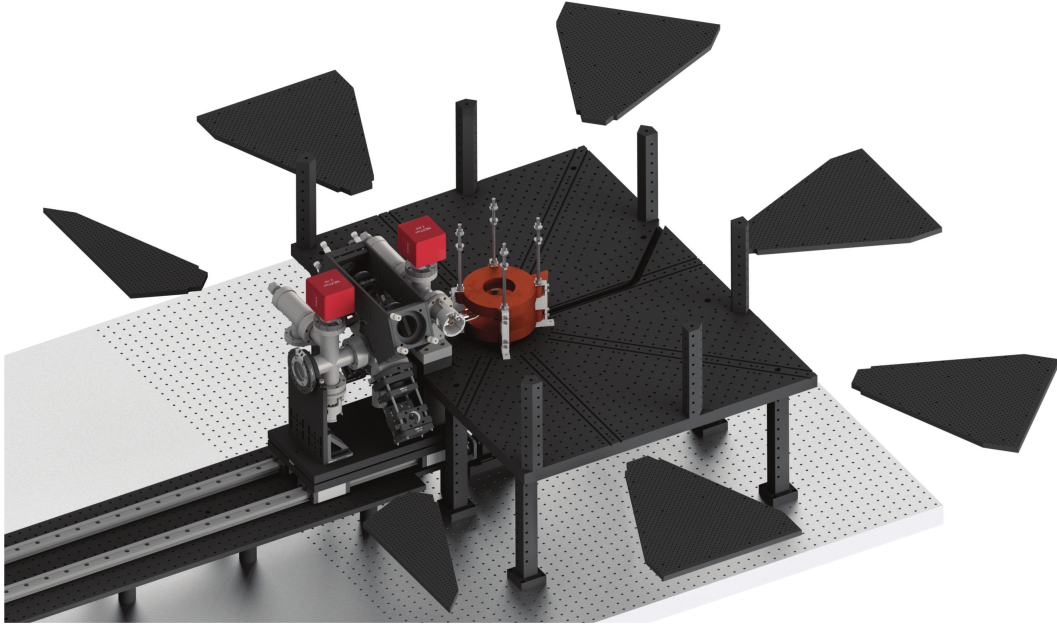


Figure 4: Mounting of the vacuum chamber. The chamber is mounted on rails allowing a translation to the left side. Under the glass cell a breadboard is mounded to host the octagonal modules. Above a second breadboard is mounted (not visible) to allow access of the upper glass cell viewport.

The precise placing of each component allows to pre-align the modules elsewhere, making them more accessible before mounting them around the glass cell.

Part I

ROAD TO 2D MOT/HOW TO GET FAST

LASERSYSTEM

Lasers have been used since their emergence in the 1960s for a wide variety of applications ranging from barcode scanning and printing on objects to cooling and imaging atoms. But of course, the same type of laser system can't be used for all applications as the requirements for each system are vastly different. While a laser power of 5 mW is sufficient for a CD-ROM driver but for example not enough for laser surgeries. This also holds for experiments with cold atoms in which cooling and trapping needs tens to hundreds of milliwatts while imaging the atoms only takes some microwatts. Selected key requirements for our case of cooling atoms are summarized here:

- High laser power (~ 1 W) for efficient and fast trapping of atoms see chapter 4
- Small linewidth of less than $\Gamma = 5.87$ MHz, the natural linewidth of the ${}^6\text{Li}$ D₂ line
- Stable intensity over time
- Tunable frequency to implement a long-term stable lock

This chapter describes a laser system fulfilling these requirements as well as how the laser frequency lock is implemented.

3.1 LASER SETUP

For the laser system the decision was made in favour of the frequency doubled laser, [Tapered Amplifier-Second Harmonic Generation \(TA-SHG\) pro](#), by Toptica. With 1 W in output power the laser system has a high power output compared to, for example, a [Tapered Amplifier \(TA\)-laser](#) at 671 nm (~ 500 mW). Also the linewidth of under 500 kHz which is significantly less than the natural linewidth of 5.87 MHz. The requirement for tunability of the wavelength is made possible by a diode laser with additional grating. Additional beams shaping and an autoalign function make the system easy to handle. What hasn't been addressed yet is the implementation of the lock and the long-term stability of the laser. In figure 5 the interior of the laser can be seen. The following section gives a short overview of the optical elements along the beam path particularly in view of locking the laser. Furthermore some characterizations of the system are shown.

3.1.1 TA-SHG

Diode Laser

The fundamental light source of the TA-SHG comes from a [external-cavity diode laser \(ECDL\)](#) with wavelength 1342 nm. Since the laser diode itself has a several

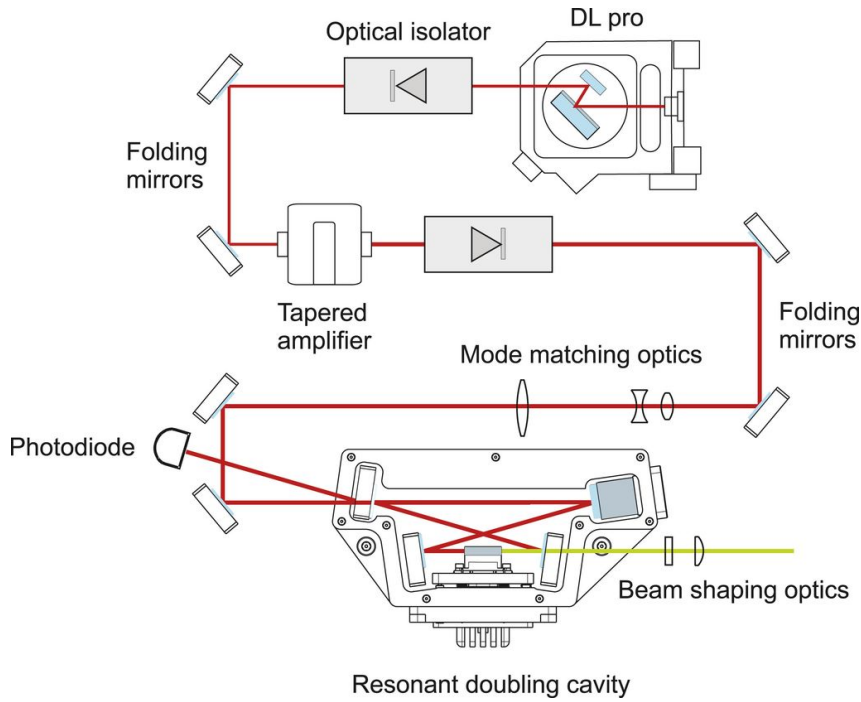


Figure 5: Interior of the TA-SHG, the red beam is in our case corresponding to a wavelength of 1342 nm, the green light leaving the **Second Harmonic Generation (SHG)** crystal is at 671 nm. Taken from [17].

nanometer broad spectrum, an external cavity is needed as it grants to select specific modes. As seen in figure 6 a blazed grating forms the external cavity by reflecting a majority of the light back into the diode and transmitting the rest as laser output. In the cavity only wavelengths which form a standing wave within the cavity length are allowed e.g. $l = n \cdot \lambda/2$. This allows a selection of the relevant mode by moving/rotating the grating. Furthermore mode hop-free frequency tuning is ensured by a feed-forward onto the laser current. Due to the broad spectrum of the original diode laser, the wavelength can be tuned over approximately 20 GHz. Behind the diode laser an optical isolator is situated to ensure no back reflection is going into the laser diode.

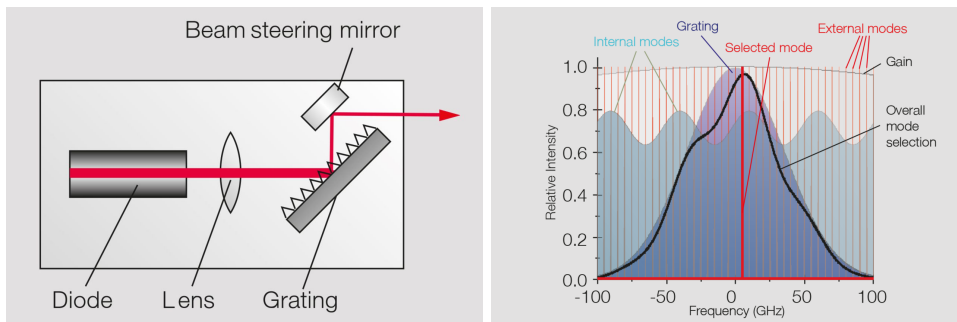


Figure 6: ECDL in Littrow configuration is shown on the right. On the left gain profiles of an ECDL, the internal modes come from the internal cavity of the diode laser itself. The external modes from the external resonator can be seen in red. Additionally the FWHM from the grating can be seen. Taken from [17].

Tapered Amplifier

TAs serve to increase the laser power. They consist of a semiconductor chip with waveguide and a tapered gain section. The waveguide only supports one propagation mode such that two remotely adjustable mirrors are needed to couple into the **TA**-chip because of the four degrees of freedom, two for the spatial position and two for the angle. The available **TA**-chip shows a higher power output in the NIR regime than for visible light. Therefore a NIR laser is used as a seed, than amplified before its frequency is doubled to 671 nm red light. Avoiding feedback from the cavity an optical isolator is placed behind the **TA**. The spatial mode is matched to the cavity mode with matching optics situated behind the optical isolator.

SHG

SHG is a nonlinear effect by which light is frequency doubled. Nonlinear in this setting meaning higher order dependence of the polarisation on the electric field. As can be seen in:

$$P(t) = \chi^{(1)}E(t) + \chi^{(2)}E^2(t) + \chi^{(3)}E^3(t) + \dots$$

the factor $\chi^{(1)}$ is known as the linear susceptibility in contrast to $\chi^{(2)}$ and $\chi^{(3)}$ denote the second- and third-order nonlinear optical susceptibilities, respectively. Second order nonlinear optical interactions can only occur in non centrosymmetric crystals. Since inversion symmetry causes $\chi^{(2)}$ to vanish. In the crystal two photons of the same frequency are annihilated by the optical material and a new photon with double the frequency is emitted. The resulting laser light is variable between 669 nm and 673 nm, depending on the wavelength of the fundamental light source.

Cavity

To enhance the **SHG** effect a bow-tie cavity is build around the **SHG** crystal. The cavity length must match a multiple of the wavelength of the ingoing beam such that constructive interference with the circulating wave can be achieved. This is done with an adjustable mirror inside the cavity. The mirror with a double piezo element can than be adjusted according to a **Pound-Drever-Hall (PDH)**-error signal. An exemplary error-signal can be seen in figure 7. The signal shows a peak at the correct cavity length. Further in the figure, effects of poor alignment of the cavity can be seen. This can be fixed by the autoalign function. For the cavity to only be resonant to the fundamental light, one of the mirrors is highly transmissive to the converted light, see figure 5. Apart from the wavelength the phase of the interacting waves has to match for efficient conversion. This can be tuned by changing the temperature of the crystal and therefore the refractive index.

3.1.2 *Characterization*

Afterwards beam shaping is done before the beam leaves the **TA-SHG**. The outgoing beam can be seen in figure 8. The output is slightly elliptical, with a ellipticity ratio of the minimum to maximum width, of 0.96 and waists of $\begin{cases} 1720.17 \mu\text{m} \\ 1787.77 \mu\text{m} \end{cases}$.

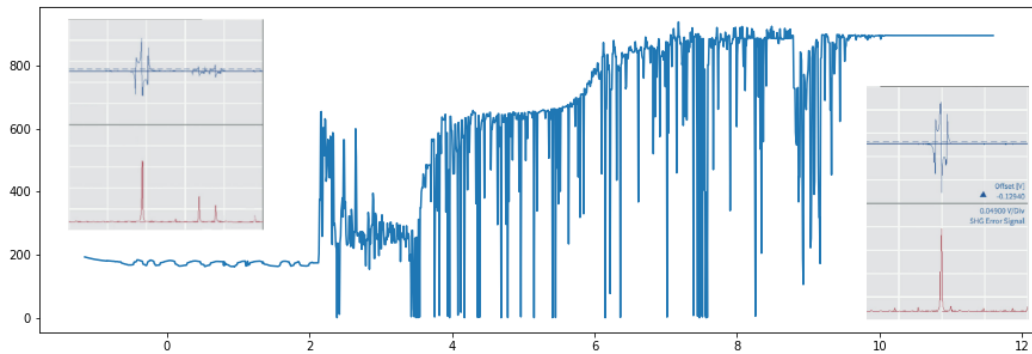


Figure 7: Autoalignment is necessary if the TA output power is changed more than 10%. Resulting misalignments become apparent in the output power and in the PDH-error signal of the SHG-cavity. The error-signal before and after autoalignment as well as the power during alignment can be seen.

Additionally the beam shows a slight convergence, seen with the shear plate as well as by measuring the beam diameter at some distance from the laser. This was corrected with a telescope consisting of a 125 mm and a 75 mm lens. Leading to a reduced waist of $\sim 1.1 \mu\text{m}$ which also improves the mode profile of the Acousto Optical Modulators (AOMs), see section 4.2.1.

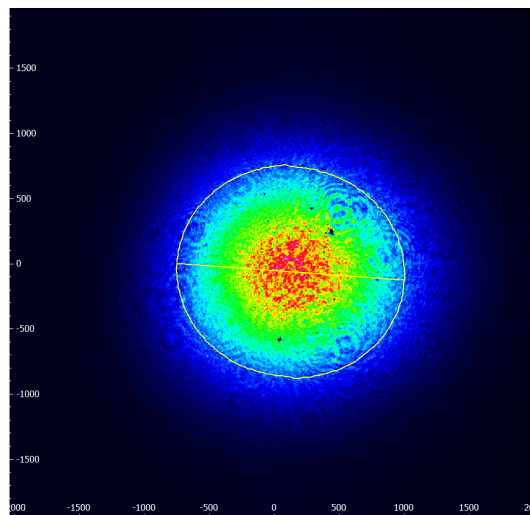


Figure 8: Beam coming out of the TA-SHG, the seen speckles come from the mounted ND filter in front.

Since this laser is one of the major light sources of the experiment, there is a particular importance for the system to be stable and robust. This is realized in the Toptica TA-SHG via temperature control, air pressure compensation as well as an autoalign function for aligning the incoupling of the TA and the cavity. Temperature variances are regulated as they lead to frequency drifts for the diode laser, modulation of the gain of the TA and stress for the SHG crystal. Further air pressure drift causes frequency deviation wherefore a compensation in piezovoltage for the grating of the diode laser is applied.

Other causes for power drift are changes in the laser diode current or the piezovoltage of the DLpro, as can be seen in figure 9. These may become relevant while

SHG power	air pressure	temperature SHG	temp. diode	temp. TA
2 mW@500 mW	5.7 mbar	0.001 °C	0.001 °C	0.001 °C

Table 1: Stability of different parameters of the laser over two days

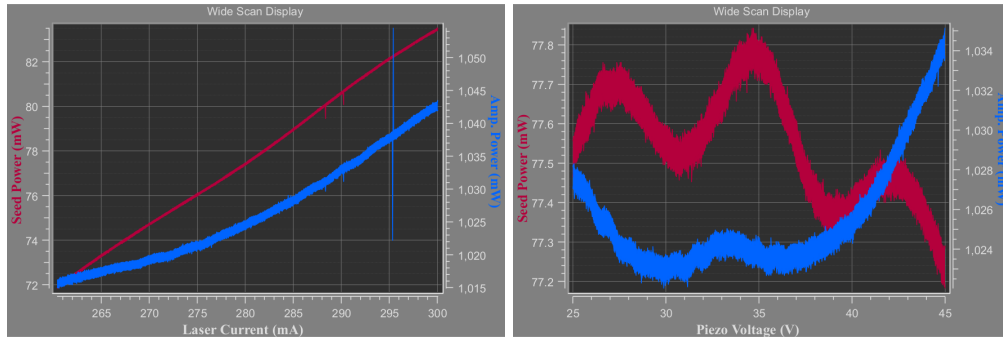


Figure 9: Seed Power and Amplifier Power depends on the laser current and the piezo-voltage.

frequency locking the laser, see section 3.2. To ensure a constant power output there is the possibility to use an implemented regulation of the TA current to compensate.

3.2 CHANGING THE FREQUENCY OF THE LASER

With the laser as it is, the frequency drifts from several MHz to a few GHz a day. While the automatic pressure compensation helps to stabilize the frequency of the laser, it still shifts more than the linewidth of the D2 transition. For this reason a laser lock is needed that continuously measures and adjusts the frequency. There are two possible ways to adjust the frequency of this laser:

1. **Piezovoltage:** As explained previously the diode laser has an external cavity grating to select a specific mode from the several nm broad spectrum of the diode laser. This selection can be altered by changing the angle of the grating. Since selection needs to be of the order of the wavelength a piezo actuator is needed, which uses the inverse piezo electric effect to create a movement depending on the applied voltage. Typically the displacement is of the order of micrometers. However, the piezovoltage can only compensate slow changes of the order of kHz or lower.
2. **Laser diode current:** Another way to change the frequency is to change the drive current going through the laser diode. This change essentially induces temperature changes influencing the thermal population of the valence and conducting band [18]. Therefore the wavelength can also be turned by varying the temperature of the diode. This effect can compensate shifts up to 20 MHz.

For a stable laser lock both options are needed. While the current compensate for high-frequency disturbances and jumps, the piezovoltage is necessary for its large wavelength tuning range and for long term drifts.

3.3 SPECTROSCOPY

To actively control the frequency of the laser a real-time errorsignal is needed. Since to cool the atoms the D2 line was chosen, it is convenient to use a lithium itself as a reference in form of a spectroscopy. In addition to Doppler-free saturation spectroscopy a frequency modulation is employed to generate an error signal. This signal is called [modulation transfer spectroscopy \(MTS\)](#) signal. The details of the spectroscopy setup can be read up in [19].

Two counter propagating laser beams are superimposed in the vapour cell filled with gaseous lithium-6 while sweeping the frequency of the laser. In case of doppler-free saturation spectroscopy both beams have the same frequency ω_L . Now two cases can happen, either $\omega_L \neq \omega_a$, with ω_a the atomic transition frequency and both beams address different velocity classes or $\omega_L = \omega_a$ then both beam address atoms of $v = 0$ m/s leading to a Lamb-Dip. This dip shows the doppler-free frequency as well as the natural linewidth of the transition.

This signal is still impractical as an error signal since it is symmetric around the dip. To be able to differentiate between red- and blue detuned light, an asymmetric error signal is needed. Here modulation of one of the beams gives us the derivative of the spectroscopy signal. With an [Electro Optical Modulator \(EOM\)](#) two sidebands with frequency $\omega_L \pm \omega_m$ are created. Compared to an [AOM](#) the [EOM](#) sidebands are collinear.

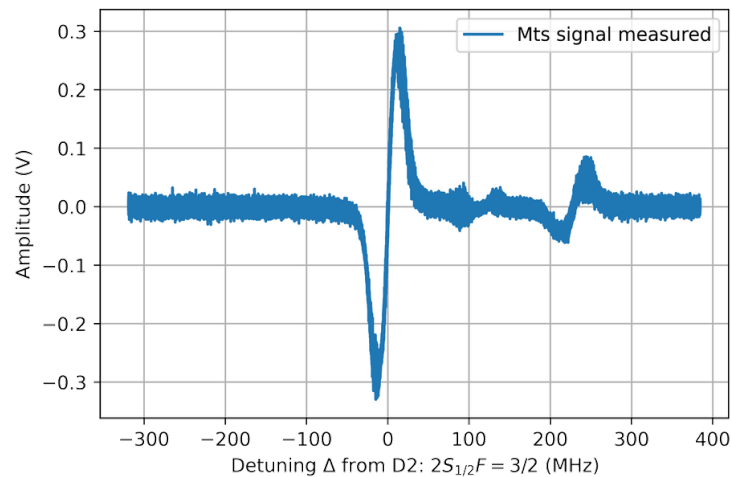


Figure 10: [MTS](#) Signal: Amplitude of the errorsignal against the detuning. The seen peaks are from the right to the left $F=3/2$, crossover and $F=1/2$.

3.4 LOCK

From the spectroscopy a reference signal is given. To control tuning of the frequency, two [PIDs](#) are used for the piezovoltage and the laser diode current. In contrast to for example the few fermion experiment in our group [20], the laser is intended to be kept stable at one frequency. This allows the light to be utilised by the other laboratories as it is independent of the dynamic needed for example to image different hyperfine states. The dynamic range for tuning the frequencies is given by [AOMs](#) (see 4.2.1) or rather a second laser for imaging.

3.4.1 *DLCpro Lock*

Toptica offers commercially available solutions for the **PIDs**. One of the options is the DLCpro Lock which is already build into the PC GUI of the laser and offers two digital **PIDs**. A **PID** controls the output value of a process corresponding to an error value $e(t)$ calculated from the difference between a designated set point and the current measurement. The correction of the feedback is applied corresponding to the Proportional K_p , Integral K_i and Derivative K_d terms of the error value. The sum of all parts $u(t)$ is then used as the overall control function.

$$u(t) = K_p e(t) + K_i \int_0^t e(\tau) d\tau + K_d \frac{de(t)}{dt} \quad (1)$$

As previously explained, the **MTS** signal can be used as an error signal and **PIDs** can be used to control the piezovoltage and the diode current. What is left is to set the coefficients of the control function. First one should check the polarity of the signal such that the direction of the scan output is the same as an increase controller output. This can be done by choosing some value for the proportional part and put the rest to zero.

The PID then can be optimized by manually tuning the parameters. One way to do so is to start with optimizing the piezovoltage PID by setting all gains to zero and then increase the integral (I) gain to a non-zero value until the control variable starts to oscillate. Here one should mind the time bases chosen to look at the control variable since the oscillation of the diode current PID will be approximately a few MHz while the piezovoltage one is on the scale of kHz. The value is halved until it doesn't oscillate any more. This is then repeated for the P and D part. Afterwards the same needs to be repeated for the diode current PID. Both **PIDs** act in parallel but with a lowpass/highpass to divide the errorsignal into a fast part and a slow part.

There is to note that this will set the parameters roughly but there is still room to improve the lock. Especially since there is a difference between a small error signal and a system robust against disturbance. A larger disturbance might throw the laser out of lock if the gains were chosen too high even if the error signal appeared to be optimized for this setting. The robustness was investigated by applying a pulse as noise to the diode current and looking at the response of the errorsignal over time, see section 3.4.3. The control bandwidth is specified to 20 kHz.

3.4.2 *Red Pitaya Lock*

Another way to lock the laser is to use a Red Pitaya STEMLab 125 – 14. Red Pitaya is a commercially available single board computer with Linux as its running system. From previous works in our group a software is available to lock the laser [20]. Essentially a FPGA was programmed and made accessible in a web interface allowing to use the chip as digital **PIDs**. The Red Pitaya offers two fast analogue-to-digital converters (ADC) as input and two fast digital-to-analogue converters (DAC) as output, all having a sample rate 125 MS/s and an resolution of 14 bit. An overview over the lock setup can be seen in figure 11.

Setting the **PIDs** is done in the same way as for the DLCpro Lock. With the difference that the **PIDs** can be either set in parallel or in series. The coarse setting of

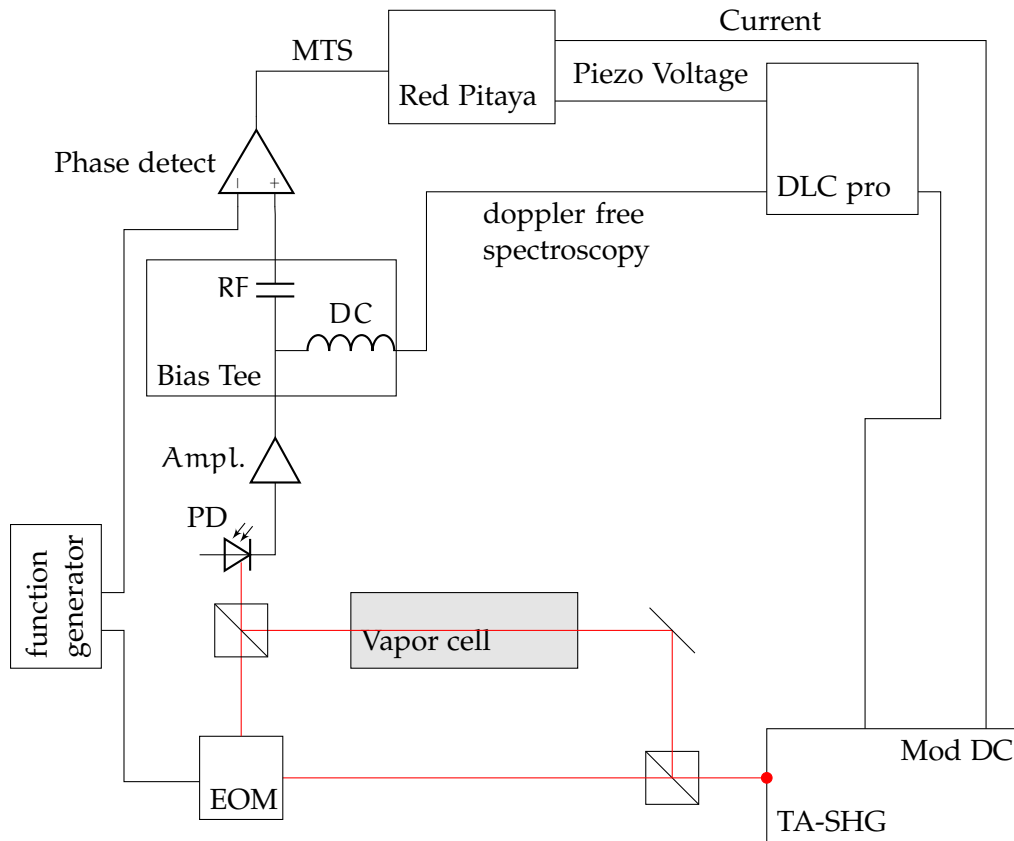


Figure 11: Scheme of the lock set up configuration for the Red Pitaya.

output	sensitivity mod DC	sensitivity piezovoltage
-1 to 1V	0.73 mA/V	1.5 V/V

Table 2: Parameters of the Red Pitaya

the piezovoltage is done on the laser itself with the dopplerfree spectrum from the DC part of the bias tee. Since the Red Pitaya hasn't such a big range or rather sensitivity lower to better fine adjust. The control bandwidth of the Red Pitaya is of the order of 1.25 MHz [20, 21] significantly higher than the 30 kHz of the DLCpro Lock. This is why Red Pitaya was used instead to lock.

3.4.3 Comparison

To compare both locks a voltage pulse was given on the laser via the analogue control of the laser current. The modulation results in a shift of the frequency. Figure 12 shows the signal from the function generator on the oscilloscope in green. The blue signal represents the pulse on the errorsignal for the case of no locking or scanning. To get a linear response the laser was set to run at a zero crossing prior to the modulation. The orange signal corresponds to the case of a locked laser. Here compared to the unlocked case after the initial disturbance a regulation is taking place. After the pulse declines, the signal becomes negative as the

PID compensates in the other direction.

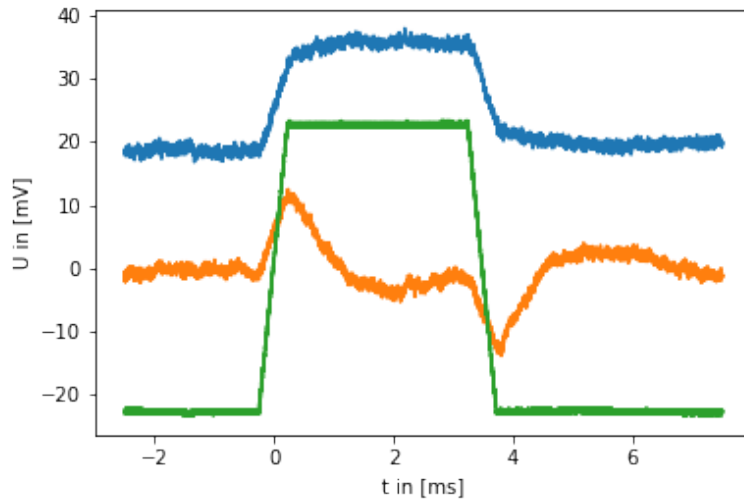


Figure 12: Adding a pulse noise to the laser current. In green the function generator signal can be seen. In blue the noise can be seen on the errorsignal for the free running case. In orange the same signal can be seen for the locked case, here with the DLCpro Lock.

By measuring the time until the signal is regulated back to the wanted transition i.e. zero, an estimate for the quality of the lock is given. This also allows to have a qualitative comparison of the locks.

Further the stability of the lock can be tested. In case of an unstable lock for example oscillations can be seen and the signal is not regulated back to the corresponding zero crossing. To ensure that the signal is regulated back to the right transition and no jump of the zero crossing has taken place, a wavemeter (high finesse wavemeter WS7) is utilized. The wavemeter has a uncertainty of 100 MHz, while it is enough to see if jumps between $F = 3/2$, crossover and $F = 1/2$ happen, since they differ about 114 MHz, it is not enough to do a direct comparison of both locks.

For optimized [PIDs](#), the DLCpro Lock needs 0.5 ms and the Red Pitaya Lock 30 μ s. While both times are lower than what is expected from the control bandwidths, the Red Pitaya is significantly better. Additional delays are the cause. For example the bandwidth of the MTS signal hasn't been considered as well as delays in the signal transportation.

The MTS signal translates frequency fluctuations into voltage fluctuations. To translate the measured voltage amplitude into the slope of the MTS signal need to be measured.

From beat note measurement with the locked laser from an other experiment the relative frequency deviation can be estimated to ~ 0.7 MHz. Further it is important that the laser remains locked over a long period of time. The current system was tested to be stable for at least 2 weeks. Longer measurements were not taken since either the connection to the Red Pitaya was lost or changes in the laser system needed to be done.

MAGNETO OPTICAL TRAP

While the last chapter was about setting up the laser lock, this chapter shows its application in our 2D- and 3D-MOT. Using a MOT, hot atoms leaving the oven are trapped and cooled. Following the transverse cooling of the atoms in the 2D-MOT, a transfer and recapture in the 3D-MOT is taking place. There the atoms can be trapped for tens of seconds at a temperature of a few hundreds microkelvins [22]. To do experiments with a deterministically prepared few particle fermionic system the trapped cold atom ensembles represent the first step.

Being trapped in the glass cell allows many access points to the sample. This presents a great advantage to tune the properties of the sample and to allow to prepare few particle systems. For instance, additional magnetic fields and optical lattices can be added. For example using optical potentials from different angles and using high numerical aperture optics as well as DC and AC magnetic fields. One example for an optical lattice is explained in the next chapter.

4.1 LASER COOLING AND TRAPPING

The theory of MOT follows two aims: laser cooling which addresses atoms of a certain velocity class via the Doppler effect and trapping of the atoms which works via the Zeeman splitting. The tools needed to realize a MOT are a laser locked to an atomic transition with an accuracy of a few MHz and a magnetic field gradient with a zero in this way, atoms are captured in real and momentum space. Note that the following explanations are for the 1D case. The 3D case can be obtained by superimposing the 1D cases.

4.1.1 Laser cooling

The cooling of atoms happens due to absorption and spontaneous emission of light. Due to conservation of energy the absorbed light leads to an increase of the internal energy of the atom causing the atom to go in an excited state. The angular momentum of light can be found in the selection rule $\Delta l = \pm 1$. Coupled with momentum conservation the linear momentum of the light causes a motion of the atom.

After an atom absorbs light and gets in an excited state it decays back to the ground state after a certain time either by spontaneous emission or by stimulated emission. Both emissions leading to different effects. While in case of spontaneous emission the photons momentum $\hbar\vec{k}$ is emitted in a random direction leading to a total momentum transfer over many excitation cycles of zero. In a stimulated emission the emitted photon moves in the same direction as the absorbed photon resulting in a net momentum of zero and no cooling. Over many cycles the force acting on the atoms can be written as

$$\vec{F} = \hbar\vec{k}\gamma_p \quad (2)$$

where γ_p is the excitation rate of atoms.

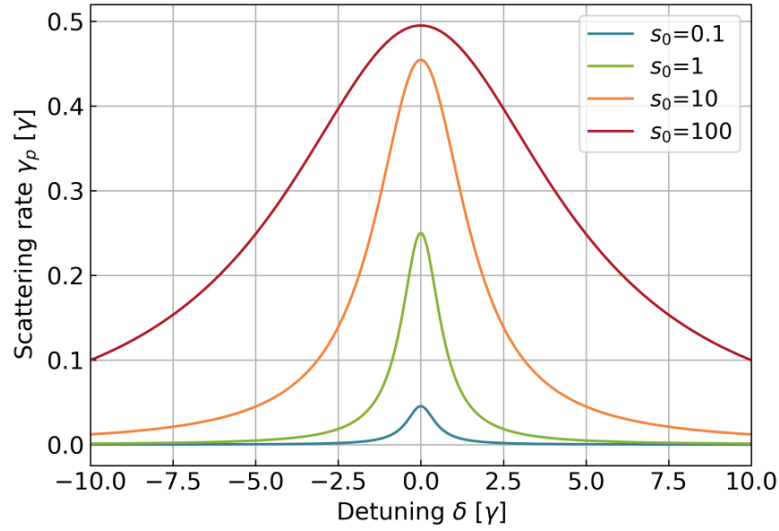


Figure 13: Scattering rate over detuning for different intensities. s_0 stands for the intensity in units of the saturation intensity I_{sat} . Taken from [16].

Another crucial factor for laser cooling is addressing the right velocity profile of the atoms. While the force currently doesn't have a velocity dependence it can be introduced through the Doppler shift $\delta_D = -\vec{k} \cdot \vec{v}$. Therefore by selecting the detuning of the laser the velocity class of the cooled atoms is selected. It is not possible to go to arbitrary detunings as a reasonable number of scattering events are needed. The number of scattering events is dependent on the intensity of the laser as can be seen in the power broadening of the absorptions curve (figure 13). For higher intensities the lasers can be further detuned.

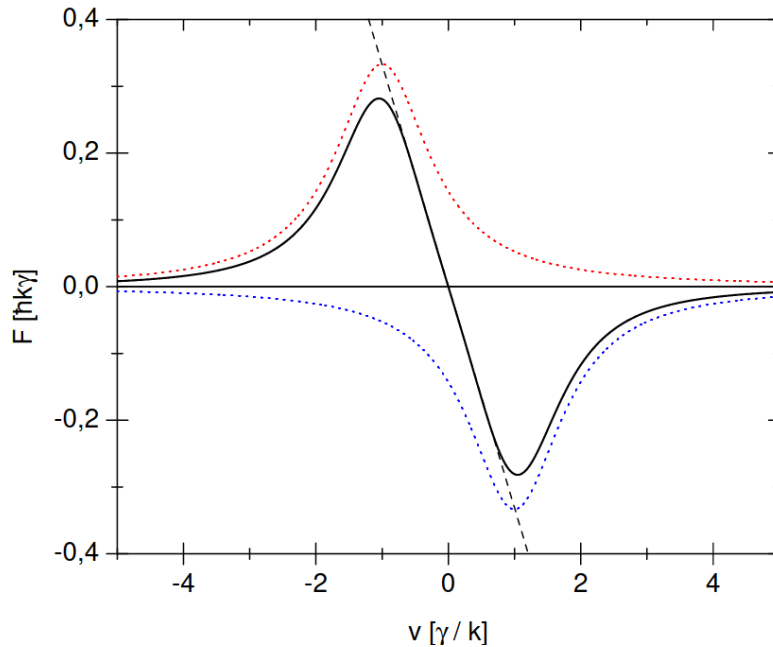


Figure 14: Optical molasses for 1-D, $s_0 = 2$ and $\delta_0 = -\gamma$. The red and blue dotted lines display the contribution of each individual beam. Taken from [22].

Until now we only considered one laser beam. To effectively cool the sample a counter propagating beam is needed to slow down the atoms independent of their moving direction. This gives rise to the so called optical molasses, as seen in figure 14. For negative detuning the force is acting against the velocity of the atom thus damping it.

4.1.2 Trapping

While the optical molasses can be used for cooling, it is not sufficient for trapping since there is no dependence on the position of the atom. This can further be seen in the optical Earnshaw theorem stating that a particle cannot be trapped solely by scattering forces [23]. Similar to adapting the force on the atoms to be velocity dependent via the Doppler shift, one can impose a position dependence via the Zeeman effect. The Zeeman effect occurs in the presence of a magnetic field yielding a splitting of the m_J manifold. Achieving a position dependence is done by applying a linear magnetic field gradient, a suitable configuration for example is an Anti-Helmholtz configuration with zero magnetic field in the middle. For the case of a total angular momentum quantum number of $J = 0$ for the ground state and $J = 1$ excited state the splitting is as in figure 15. Exciting the atoms to the $m_J = -1$ -state happens with matching polarisation in this case a σ^- -polarized beam. Thus from both sides σ^- light is send in. The detuning of the laser beam δ_0 then determines the positions $\pm R_c$ where the atoms are resonant. For example the beam coming from the left side excites the atoms at $z = -R_c$ to the $m_J = -1$ state, pushing them towards the centre of the trap. Behind the centre the quantization axis is flipped, therefore the polarisation inevitably needs to be flipped as well. Thus, the beam coming from the left can't interact with the atoms on the right hand side. For this a σ^- beam from the right side is necessary, causing the atoms to be trapped within $\pm R_c$.

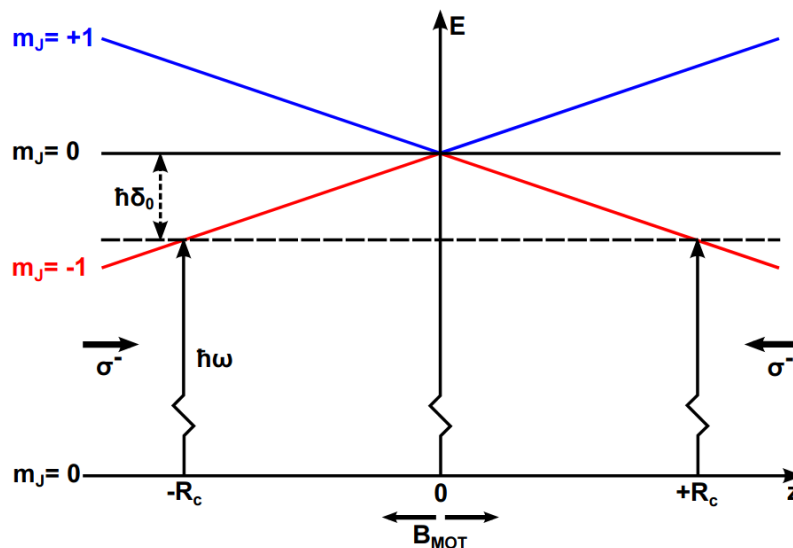


Figure 15: The applied magnetic field and the corresponding Zeeman splitting is visualized. The polarisations of the beams is shown in direction of the beam. Taken from [22].

4.1.3 Cooling in ${}^6\text{Li}$

As previously mentioned, we use the D2 line, between $2^2\text{S}_{1/2}$ and $2^2\text{P}_{3/2}$ of ${}^6\text{Li}$ (figure 16) to cool the atoms rather than the D1 line. Since the natural linewidth of this transition with 5.9 MHz is bigger than the hyperfine splitting of the $2^2\text{P}_{3/2}$ state $\Delta E = 4.4$ MHz the splitting can't be resolved. Therefore the transition from the $F = 3/2$ state is not closed. As a result, a second transition from $F = 1/2$ is needed to close the cycle and two different laser wavelengths are needed. Both transitions have approximately the same strength allowing a power splitting of 50 : 50 between both frequencies.

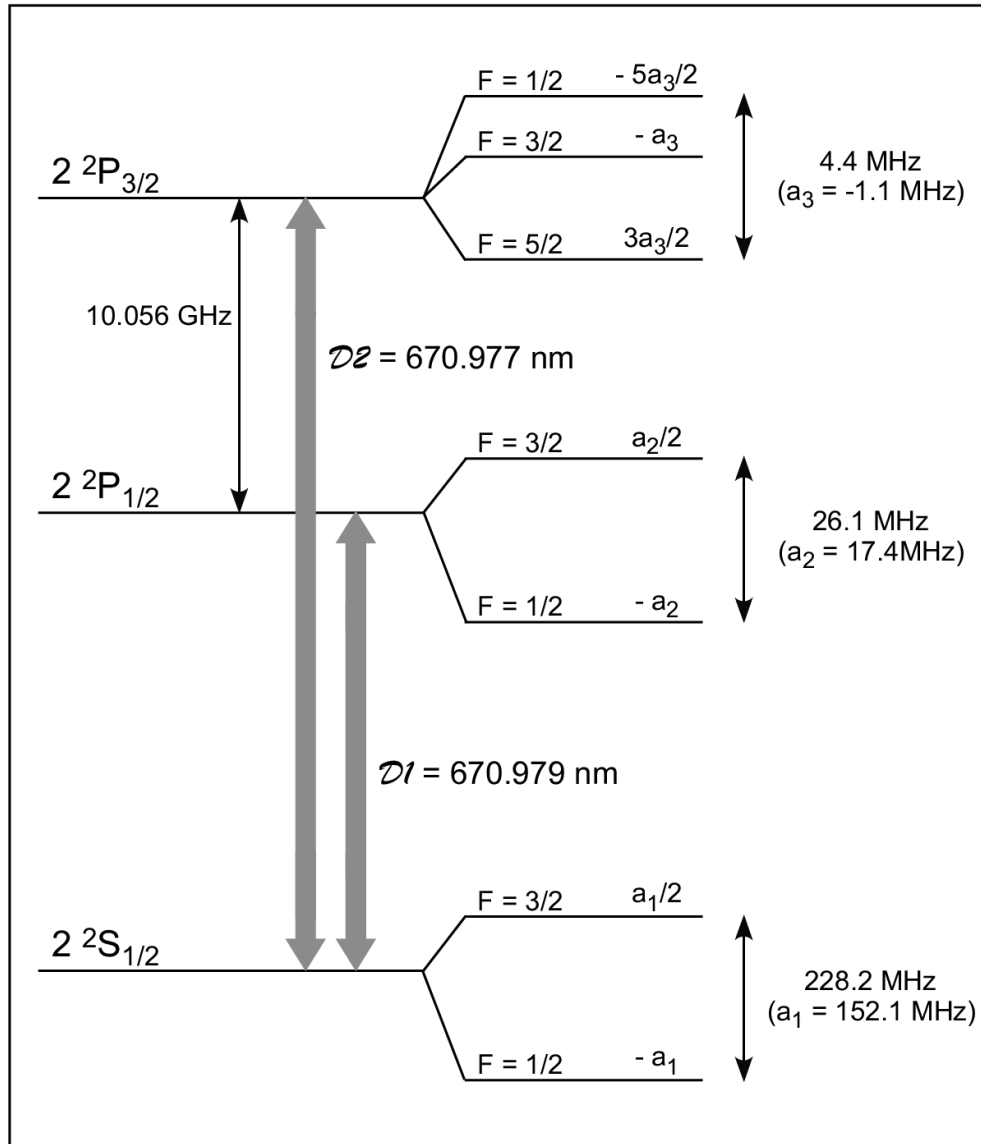


Figure 16: Energy levels of Lithium-6. Shown are the ground and excited state as well as the different hyperfine splittings. Taken from [24]

4.2 SETUP DISTRIBUTION

The optical distribution and frequency shifts of the TA-SHG light are done in free space. The modified light is then coupled into fibers which are taking the light to the experiment table. For the optical setup some basic rules are followed according to the concepts of [HQA](#) to acquire a system which allows a predetermined and modular setup:

- Height: All optics are mounted such that the optical component is at 50 mm height.
- Positioning: The beam path is led such that it always lays over the row of holes of the underlying breadboard and is hence naturally centred to the glass cell viewports

These reductions of degrees of freedom makes it easier to characterize the beam or to add additional component especially as passive alignment is further simplified with alignment tools [19].

In this section an overview of the laser distribution, its components and how to ensure the frequencies is described.

4.2.1 Doublepass

Since lithium doesn't have a closed transition for cooling, two separate frequencies for the [MOT](#) are needed. To shift the frequency of the laser for the cooler and repumper beams [AOMs](#) in doublepass configuration are used. Additionally the spectroscopy is frequency shifted, leading to an opposed frequency shift of the laser itself, to allow a better dynamic range for the [AOMs](#). The locking scheme is visualized in figure 17. This section explains what an [AOM](#) doublepass is and how to align the three doublepass modules.

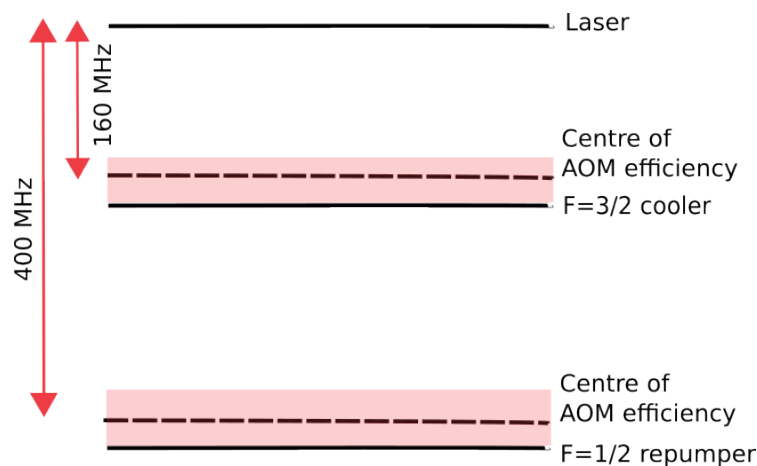


Figure 17: Locking scheme of the laser setup. The laser frequency is shifted from $F=3/2$ via a doublepass. Two additional doublepasses are used to shift the frequency for the cooler and repumper. Highlighted with red box are the dynamic ranges of the [AOMs](#).

[AOMs](#) consist of a transparent crystal, where by applying an oscillating volt-

age to a piezo stack, an acoustic wave is induced. This leads to a spatial deflection of the laser beam going through, as well as a frequency shift according to $f = f_l + n \cdot f_{\text{Voltage}}$. The doublepass configuration can be seen in figure 18. A s-polarized beam is reflected into the AOM and deflected in different orders. Behind $\lambda/4$ waveplate a lens is situated a focal length away from the centre of the AOM leading to parallel focused beams. With an iris the 1st order can then be selected. The mirror situated at focal length is used to overlap the reflected beam with the ingoing beam and being collimated after passing the lens a second time. Due to going through the $\lambda/4$ waveplate twice the beam polarisation can be rotated 90° allowing the Polarizing Beam Splitter (PBS) behind the AOM to separate the ingoing from the outgoing beam. Going into the AOM the second time with the same angle causes the beam to be diffracted in the other direction cancelling the angle. Here a second iris is needed to again block the unwanted orders. This allows us to continuously fine tune the frequencies without realigning the optics. In accordance with the idea of the experiment this was implemented as a module. Here the degrees of freedom are restricted to only the necessary ones. Details of the planning of the module and comparison to a free space configuration can be found in [25].

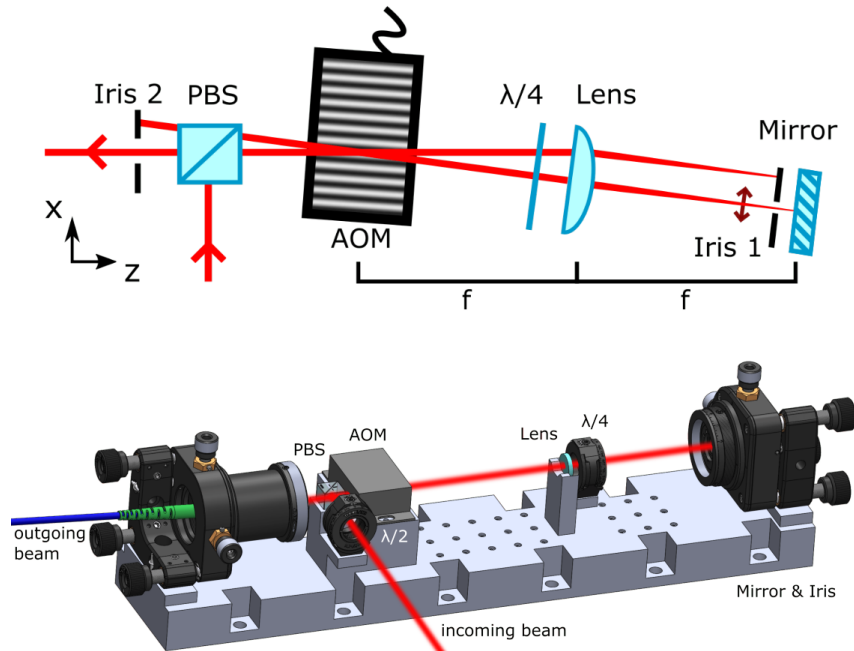


Figure 18: Schematic drawing of a doublepass AOM setup as well as a picture of the doublepass AOM module. Taken from [25].

The module is intended for a beam height of 50 mm and an ingoing beam along the hole row. It allows to select the first diffraction order. If the -1st is needed, the socket for the AOM needs to be turned by 180° . The alignment of the doublepass is done with the following few steps:

- free space beam is aligned with two mirrors to the hole line as well as to the opening of the AOM

- rotate the **AOM** such that over 90% is in first order, for this there is a pin in the module around which the **AOM** can be rotated
- align mirror mount such that beam is retro reflected/ power maximal after doublepass
- turn $\lambda/4$ plate until the outgoing power is optimized

In the current setup the three double passes have the following components:

Frequency	Lens(Coating+focal lens)	AOM
80 MHz	$f = 84$ mm	G&H 3080-1214
200 MHz	$f = 54$ mm	G&H 3200-1214

Table 3: Components of the doublepass modules

4.2.2 Distribution

The optical setup directly behind the TA-SHG can be seen in figure 19. The outgoing laser beam of the TA-SHG comes out at a height of ~ 75 mm. As one of our requirements for the optical setup is that the beam height is constant at 50 mm, a periscope is needed after the TA-SHG. Because of the slight defocus of the beam leaving the laser, as mentioned in section 3.1.2, a telescope is situated behind the periscope to compensate the convergence of the beam and to reduce the waist. Along the beam path, the first **PBS** (PBS1) allows to regulate the power between the free port and the experiment. PBS2 is used to regulate the power for the spectroscopy, while PBS3 is to tune the splitting of the cooler and repumper. The order of magnitude of power in each beam behind the fiber can be seen in figure 19. The light coupled in the fibers is approximately 60%.

To shift the frequencies three doublepass modules are used. One for the spectroscopy and the other two for the cooler and repumper. The prospective frequencies can be found in figure 17.

Port	Frequency	Efficiency doublepass
Spectroscopy	80 MHz	74%
Cooler	80 MHz	76%
Repumper	200 MHz	61%

Table 4: Efficiency of the different doublepass modules.

In each module the beam is going in through the reflected port of the **PBS** such that the outgoing beam has a cleaner polarisation as it is transmitted through the cube. Additionally the requirement of having a cooler as well as a repumper in the same beam path asks for a possibility to overlay both beams in order to couple them into the same fibers. Here a 50 : 50-**NPBS** is utilized to combine both beams. Overlaying the beams is done by two mirrors respectively, to ensure that both beams are laying on top of each other, both are coupled into the same fiber, later

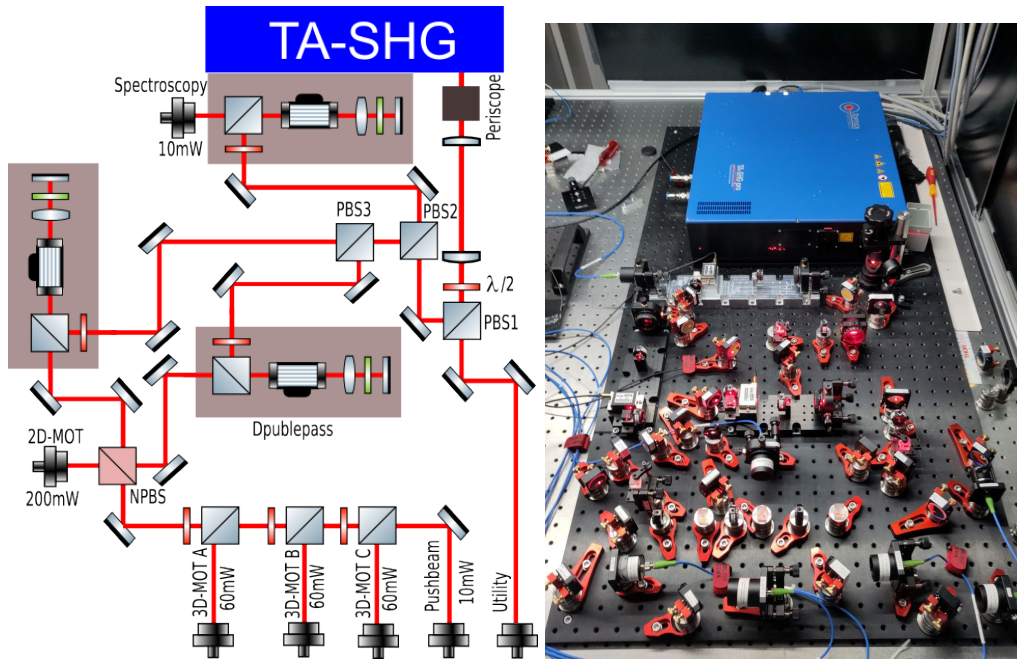


Figure 19: Laser light distribution. On the left the schematic drawing can be seen. Highlighted in grey are the doublepass modules. On the right a photo of the actual distribution can be seen.

used for the 2D-MOT. This already sets the power for the 2D-MOT. The remaining beam can be split up for the three arms of the 3D-MOT as well as the pushbeam.

4.2.3 Beat note

To ensure that the frequencies of the repumper and cooler beam are at the right frequencies a beat note with the spectroscopy light of the other experiments was set up. The beat note is acquired by overlaying two beams. If both beams have different frequencies there will be a beat, which can be measured using a photodiode and analysed by doing a Fourier transformation to acquire the frequency difference. Here some points need to be noted:

- The bandwidth of the photodetector must be high enough such that optical frequency difference is within it, in our case around 300 MHz
- The spatial distributions of the two laser beams must overlap
- The polarisation states must not be orthogonal

Additionally to the frequency differences to the $F = 3/2$ peaks appear at the applied frequencies of the AOMs. The beat signal can also be used to check the stability of the lock compared to the one in the other experiments.

4.3 MOTS

4.3.1 2D-MOT

A 2D-MOT compared to a 3D-MOT traps the atoms only in two dimensions leaving one dimension unconfined. The unconfined axis is used to transfer the atoms from the 2D-MOT to the glass cell. This results in a cigar shaped atom cloud in comparison to the round cloud of a 3D-MOT.

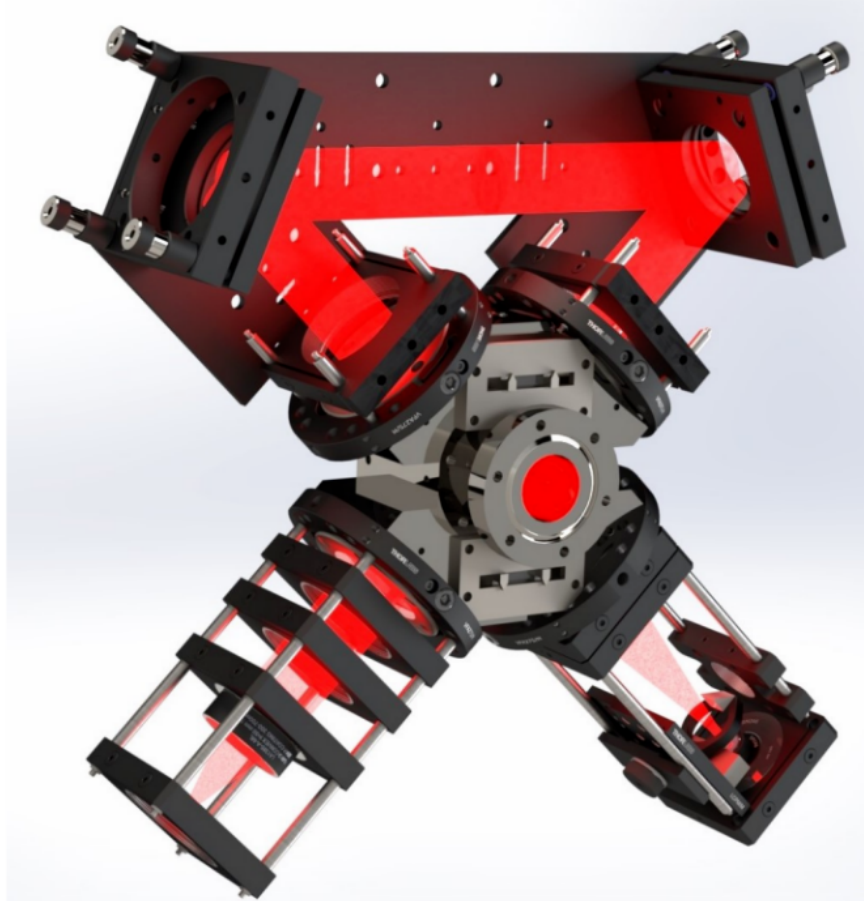


Figure 20: 2D-MOT chamber with 4 arms around the chamber. The beam enters in the bottom right arm and gets reflected in the upper arms, before being reflected in itself in the lower left arm. This configuration is called bow-tie. On the front above and below the CF40 flange permanent magnets are mounted. Taken from [16].

In figure 20 the 2D-MOT in bow-tie configuration can be seen. The goal of the 2D-MOT is to have as much atom beam flux as possible. For this high laser intensities are necessary [16, 26]. One laser beam for all four viewports is used to exploit the available power more efficiently. In figure 20 the laser beam is going from the lower right arm through the chamber here it is reflected and re-enters the chamber on the upper right corner. In front of the mirrors polarisation is changed with $\lambda/4$ and $\lambda/2$ waveplates such that it is linear on the mirrors and circular according to the magnetic field directions in the chamber. The polarisation needs to be linear on the mirrors to ensure that no additional phase shift is imposed on the polarisation

during the reflection. Further back, there is a third mirror which reflects the beam into itself including passing a $\lambda/4$ plate twice such that it passes the whole apparatus again. In front of the fiber a PBS is placed, the ingoing light from the fiber is fully transmitted, the back reflected light however is reflected out of the path since the polarisation perpendicular to the ingoing. Thus, the reflected light can be dumped and the fiber is not damaged. The current setup works with a Gaussian beam, in the future a speckled flat top, created by a diffuser, will be tested. For a Gaussian beam profile clipping occurs, among other things, on the viewports due to their flanks falling too slow. Therefore a higher loading rate might be archived with a flat top profile. More details and calculations to that can be found in thesis [27].

To align the beams of the 2D-MOT, such that they are centred and not clipping as well as nicely reflected into itself, the mirrors need to be adjusted. To do so the screw position of the mirrors was read out of the CAD file and tuned accordingly. The mirrors are then close to 45° and 90° respectively. After that the fine alignment was done by adjusting each mirror to two iris along the intended beam path in front of the next mirror. This adjustment procedure converged quickly as the screws needed to be turned only slightly.

With the optical components in place and the frequencies fixed, we still need to ensure that atoms are present. For the first test the oven was heated to 400°C . Fluorescence of the atoms allows to see the atoms with the bare eye. To differentiate between scattered light from, for example the viewports and fluorescence, the frequency of the laser was scanned in a range of about 1 GHz to find the atoms. During the sweeping the atoms "blink" as the frequency is ramped over the fluorescence range. Further the fluorescence makes the beam visible and allows to differentiate between the beam coming out of the fiber and the retroreflected one. The atoms leaving the oven move upwards, leading to the beam coming from the bottom right to be blue detuned to the resonance and the beam from the top left to be red detuned. One blinking when the scan is on the red-detuned side of the resonance and one when it's on the blue detuned side. Now it is possible to overlay them by using small beams.

The magnetic field is produced with four stacks of six permanent magnets each (see figure 20). With all in place the 2D-MOT could be seen as in figure 21.

Now all that is left is to fix the magnetic field. The alignment of the zero crossing of the magnetic field and with it the position of the atom cloud can be changed by moving the permanent magnets position via mounting plates. In the end the atom cloud should be positioned in line of sight with the differential pumping tube to allow to transfer the atoms to the 3D-MOT.

Spectroscopy	Cooler	Repumper
99 MHz	86 MHz	200 MHz
0Γ	4.4Γ	4.4Γ

Table 5: Detunings optimized for the 2D-MOT

Since the atom cloud is unrestrained along the pushbeam axis the cloud adopts a cigar-like shape. To measure the number of trapped atoms an imaging along one of the 2D-MOT axis is needed. Currently a side imaging is not possible because of stray light coming from the viewports. Therefore the detunings were optimized ac-

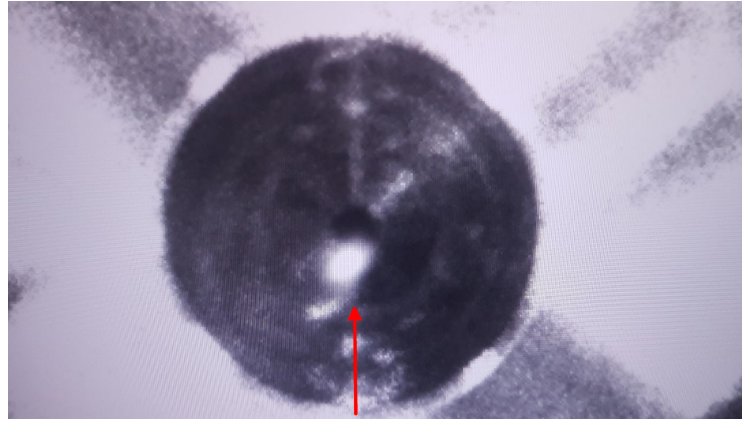


Figure 21: Picture of the 2D-MOT along the pushbeam viewport. The atoms cloud is marked by the arrow. Behind the 2D-MOT a small black circle can be seen indicating the differential pumping stage. In the optimal case they should be one above the other.

According to the pushbeam image. A more qualitative estimation will be done once the 3D-MOT is set up. The final frequencies for the MOT can be seen in table 5.

4.3.2 3D-MOT

The 3D-MOT is built around the glass cell with the coils for the magnetic field being mounted as described in the experimental setup chapter. The polarisation and the magnetic field directions are corresponding to the 2D-MOT. Finding the 3D-MOT was highly dependent on the 2D-MOT alignment. Here it needed to be ensured that the untrapped axis is well aligned with the differential pumping stage and glass cell situated behind as small misalignments of the 2D-MOT, meant the atoms being dumped in the DPS, not reaching the 3D-MOT capture volume.

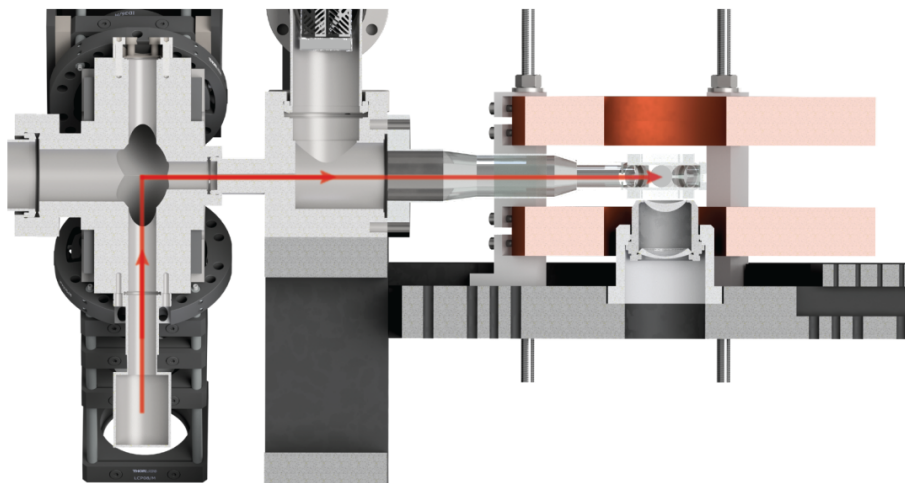


Figure 22: Atom path from the oven, the 2D-MOT through the differential pumping stage to the glass cell. Below the glass cell the objective mount can be seen as well as the coils above and below. Taken from [6].

The path for the atoms from the oven to the 2D-MOT and finally the 3D-MOT can be seen in figure 22. With the alignment of the 2D-MOT as described in the previous section, the 3D-MOT was seen as in figure 23. The atom cloud is 1.5 mm above the glass cell centre. This will be adjusted with spacers lifting the vacuum chamber. It can now be used to determine and optimize the atom number in the trap as well as the loading rate by adjusting the detuning, magnetic field and pushbeam.



Figure 23: Picture of the 3D-MOT seen from a viewport of the glass cell.

Part II

ACCORDION LATTICE/PLANNING OF A MODULE

ACCORDION LATTICE

In the introduction a motivation was given for why changing the dimensionality of a system can be of interest. How in particular the transition from a 3D to quasi-2D system comes about will be topic of this chapter. At [HQA](#) the experimental implementation is realized with an optical accordion lattice. It consists of two laser beams intersecting at a tunable angle. This way controlling the spacing between the interference fringes, and therefore the strength of the confinement of our atoms, effectively freezing out one dimension. It allows to reliably load the atoms into the central fringe at large spacing and then decreasing the spacing, effectively compressing the atomic cloud. Such dynamic optical accordion lattices have been implemented since the mid 2000s in various groups and forms [28–30]. Of explicit interest is building a miniaturized version of an accordion lattice to use in a modular way. Made possible due to a high NA objective with small aperture enabling the necessity of only small beam separations.

As discussed earlier, the deterministic 2D spilling procedure plays an incremental role in the preparation of high-fidelity few atom samples. However, the precise interplay between B-field gradients in different directions and the trap frequencies of the confining optical potential keep opening questions about the microscopic theory describing the process. Hence, an accordion lattice gives the opportunity to investigate and optimize the aspect ratio, by changing ω_z while keeping ω_r constant, for 2D spilling. The spilling is done by applying a magnetic field gradient to tilt the potential barrier and allow the atoms to spill out. This is further visualized in figure 24.

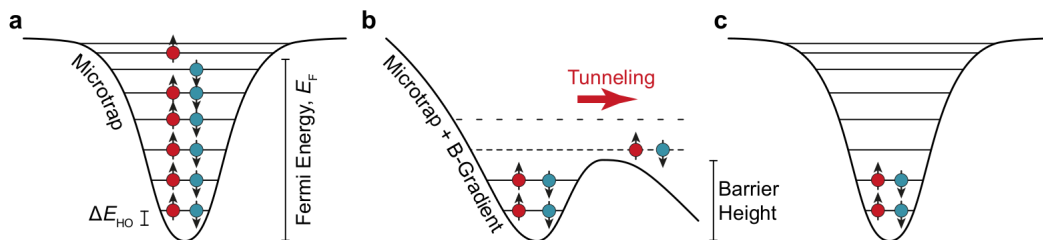


Figure 24: 1D spilling, 2D spilling similar.

- a: Micro Trap generating a harmonic potential with fermions trapped inside, b: By overlaying a magnetic field gradient, the potential barrier is tilted. The high energy level spill and only a few states with low energy remain,
- c: Few-body state with deterministic particle number. Taken from [5].

In the current experiments of our group the 2D confinement is reached by a standing wave trap, effectively an accordion lattice with fixed angle of intersection. Thus making it impossible to change the aspect ratio. The idea for the accordion lattice is to be able to examine all settings in-between both experiments.

Experiment	ω_r	ω_z	$\frac{\omega_z}{\omega_r}$	waist on atoms	spacing
few fermion [31]	$2\pi \cdot 414$ Hz	$2\pi \cdot 29$ kHz	70	$133 \mu\text{m}$	$4.19 \mu\text{m}$
2D lattice [5]	$2\pi \cdot 18$ Hz	$2\pi \cdot 7$ kHz	350	$600 \mu\text{m}$	$4.4 \mu\text{m}$

Table 6: Setting for the 2D spilling from the different laboratories in our group. The biggest difference being the factor 5 between the aspect ratios.

5.1 THEORY AND SIMULATIONS

The theory of an accordion lattice can be understood by interference of electric fields. It is adapted in parts from [31]. In this derivation particular attention is given to effects of mismatched polarisation and power splitting between the beams as well as potential sources of an asymmetric lattice.

Starting with a complex electric field of the form

$$\vec{E} = \vec{\epsilon} \cdot E_0(x, y, z) \cdot \exp(i(\vec{k} \cdot \vec{x} - \omega t + \Phi)) \quad (3)$$

with $\vec{\epsilon}$ the polarisation, $E_0(x, y, z)$ the real field amplitude, \vec{k} the wave vector, ω the frequency and Φ the phase. $I = |\vec{E}|^2 = |E_0(x, y, z)|^2$ is the intensity of one beam.

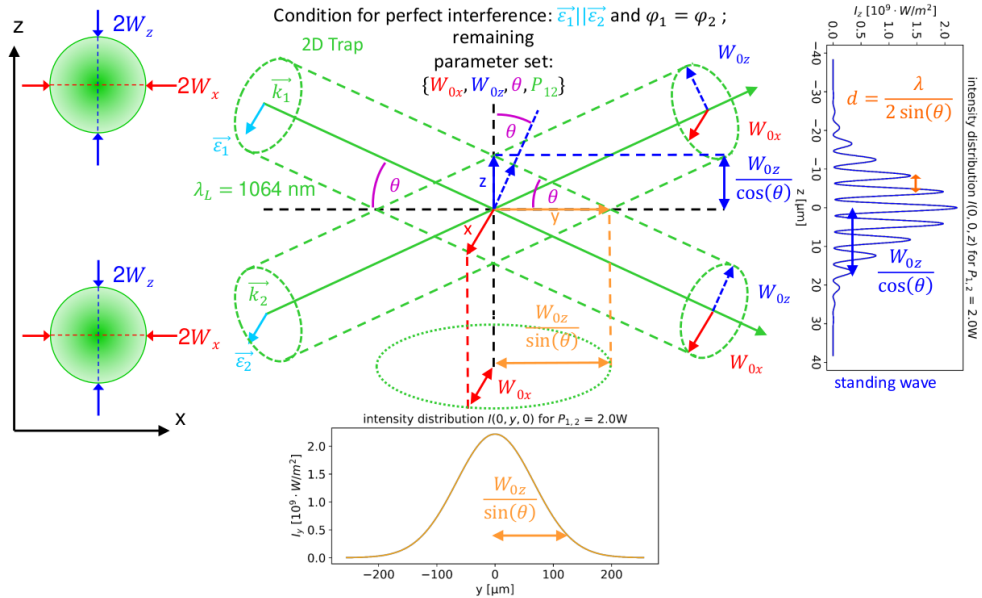


Figure 25: Two Gaussian beams intersecting at a half angle of θ . On the right side the emergent interference is pictured. In the lower picture the intersection profile perpendicular to it can be seen. Taken from [31].

In the case of two beams crossing each other interference can happen if both beams have the similar frequency ω . The intensity distribution is then:

$$I_{\text{tot}} = |\vec{E}_1 + \vec{E}_2|^2 = |\vec{E}_1|^2 + |\vec{E}_2|^2 + \vec{E}_1^* \cdot \vec{E}_2 + \vec{E}_1 \cdot \vec{E}_2^* \quad (4)$$

$$= I_1 + I_2 + \sqrt{I_1} \sqrt{I_2} \vec{\epsilon}_1^* \vec{\epsilon}_2 \exp(i((\vec{k}_2 - \vec{k}_1) \cdot \vec{x} + \Phi_2 - \Phi_1)) \quad (5)$$

$$+ \sqrt{I_1} \sqrt{I_2} \vec{\epsilon}_1 \vec{\epsilon}_2^* \exp(i((\vec{k}_1 - \vec{k}_2) \cdot \vec{x} + \Phi_1 - \Phi_2)). \quad (6)$$

Assuming linear polarisation the complex conjugation of ϵ is irrelevant. Which leads us to:

$$I_{\text{tot}} = I_1 + I_2 + 2\sqrt{I_1}\sqrt{I_2}\vec{\epsilon}_1\vec{\epsilon}_2\cos((\vec{k}_2 - \vec{k}_1) \cdot \vec{x} + \Phi_2 - \Phi_1). \quad (7)$$

In this setting the propagation direction of the wave-vectors are (see figure 25):

$$\vec{k}_1 = k \cdot (0, \cos(\theta), -\sin(\theta)), \quad (8)$$

$$\vec{k}_2 = k \cdot (0, \cos(\theta), \sin(\theta)). \quad (9)$$

This leads with $\Delta\Phi = \Phi_2 - \Phi_1$ and $k = \frac{2\pi}{\lambda}$ to:

$$I_{\text{tot}} = I_1 + I_2 + 2\sqrt{I_1}\sqrt{I_2}\vec{\epsilon}_1\vec{\epsilon}_2\cos\left(\frac{4\pi}{\lambda}\sin(\theta)z + \Delta\Phi\right) \quad (10)$$

from this the layer spacing can be read of as:

$$d = \frac{\lambda}{2\sin(\theta)}. \quad (11)$$

from eq.11 one directly sees the intimate connection between the lattice spacing and the angle of interference between both beams. What is left is to define the intensity profile. These are defined here as elliptical Gaussian beams giving rise to an intensity profile of the form:

$$I_{\text{Gaussian}} = \frac{2P}{\pi \cdot w_x(y)w_z(y)} \cdot \exp\left(-\frac{2x^2}{w_x^2(y)} - \frac{2z^2}{w_z^2(y)}\right). \quad (12)$$

with w_i being the waist in the respective direction. The beams need to be rotated around the x-axis to intersect according to figure 25. Such that the intensity distributions can be written as:

$$I_1 = \frac{2P}{\pi \cdot w_x(y)w_z(y)} \cdot \exp\left(-\frac{2x^2}{w_x^2(y)} - \frac{2}{w_z^2(y)}(\sin(\theta)y + \cos(\theta)z)^2\right), \quad (13)$$

$$I_2 = \frac{2P}{\pi \cdot w_x(y)w_z(y)} \cdot \exp\left(-\frac{2x^2}{w_x^2(y)} - \frac{2}{w_z^2(y)}(-\sin(\theta)y + \cos(\theta)z)^2\right). \quad (14)$$

Optimal contrast is reached if the polarisation is parallel to x-axis leading to $\epsilon_1 \cdot \epsilon_2 = 1$. Finally the intensity is:

$$I_{\text{tot}} = I_1 + I_2 + 2\sqrt{I_1}\sqrt{I_2}\cos\left(\frac{2\pi}{d}z + \Delta\Phi\right). \quad (15)$$

In an ideal case the power splitting between the beams is 50 : 50, this gives a maximal interference contrast for the lattice. The interference contrast of the lattice is given by:

$$v = \frac{I_{\text{max}} - I_{\text{min}}}{I_{\text{max}} + I_{\text{min}}}. \quad (16)$$

Which according to equation 15 yields

$$v = \frac{2\sqrt{I_1 \cdot I_2}}{I_1 + I_2} = 2\sqrt{\frac{I_1}{I_{\text{tot}}} \cdot \frac{I_2}{I_{\text{tot}}}}. \quad (17)$$

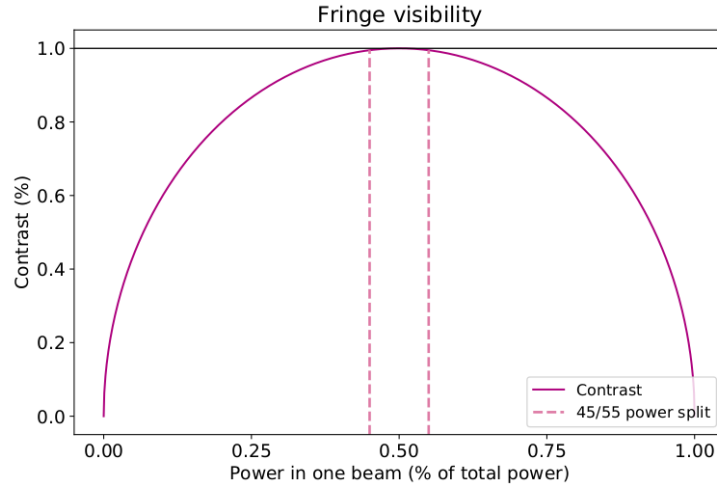


Figure 26: The contrast in dependence of the power percentage in each beam. The marked splitting of 45 : 55 corresponds to a contrast of 0.99. Taken from [32].

This is visualized in figure 26. There, it can clearly be seen that even for small deviations from the 50:50 splitting the contrast can go down substantially. Similarly the interference contrast can be off due to the polarisation. If the polarisations of both beams aren't parallel there is a prefactor < 1 in front of the cosine term (see equation 10). Previously it was mentioned that the optimal polarisation is linear polarisation along the x-axis. While it might seem as if linear polarization along the z-axis leads to the same contrast this is not the case since the lens introduces an angle between the polarisation of both beams. This becomes more apparent by performing the same polarisation on the polarisation vector as was done on the wave vector.

$$\begin{pmatrix} p_x \\ 0 \\ p_z \end{pmatrix} \rightarrow \begin{pmatrix} p_x \\ \pm \sin(\theta) p_z \\ \cos(\theta) p_z \end{pmatrix} \quad (18)$$

This gives a prefactor to the interference of $p_x^2 + (\cos^2(\theta) - \sin^2(\theta))p_z^2$. The main difference between both effects on the contrast is that the polarisation gives rise to a dependence on θ . Looking at figure 27 this effect seems to be small. A bigger impact can be seen by assuming both beams have unequal polarisation.

Additionally to imperfections of the pattern due to deviations in contrast, misalignments may occur due to shifts of the intersection point relative to the focus point. Common source of the shifts are for one angles between the beams e.g. no perfect parallelism after the beam separation or tilts of the optical elements thereafter. These effects are visualized in figure 28. The first row shows the interference pattern for a perfect alignment. Both beams intersect at the focus positioned at $z = 0$. In the second row the upper beam is shifted while the lower beam remains unchanged. Here a phase shifts occurs e.g. the position of the fringes changes. Further the intensity of the fringes changes, this can be seen in the asymmetry of the pattern. In the last row the intersection point is shifted in y-direction. In case of a large shift both beams no longer overlap in the focus leading to no interference. For small shifts again an asymmetric pattern can be seen.

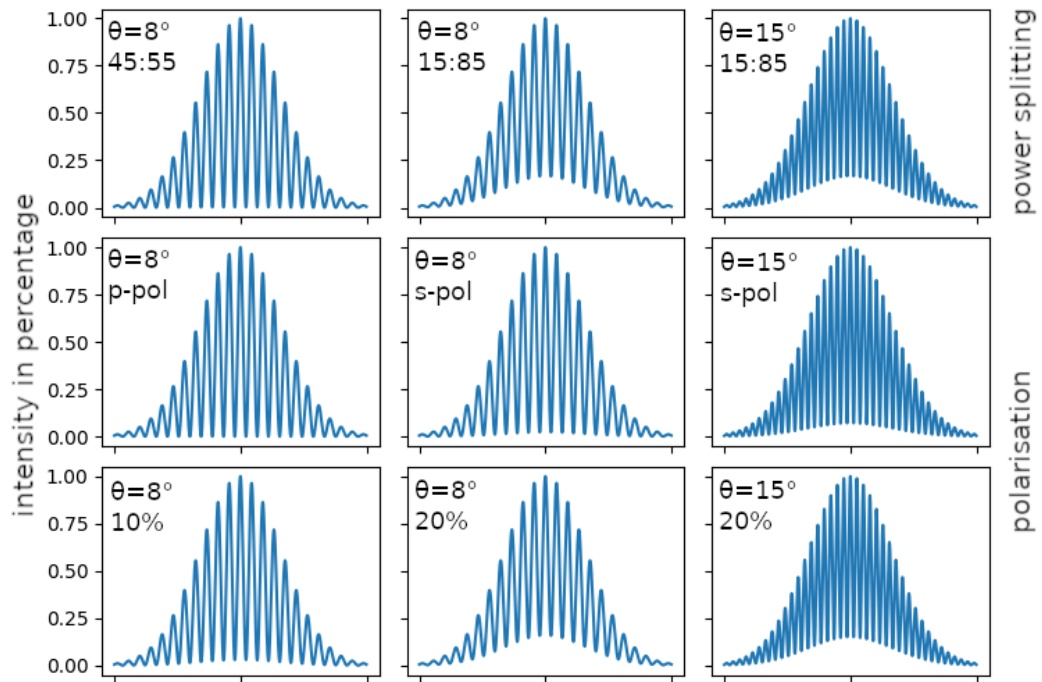


Figure 27: Simulation of different effects on the contrast. The first row visualizes the effect of different power splittings. In the second row the polarisation of both beams is equal, but along different axis. The last row shows the contrast for a mismatched polarisation between the beams, with 0% being parallel polarisation and 100% being orthogonal.

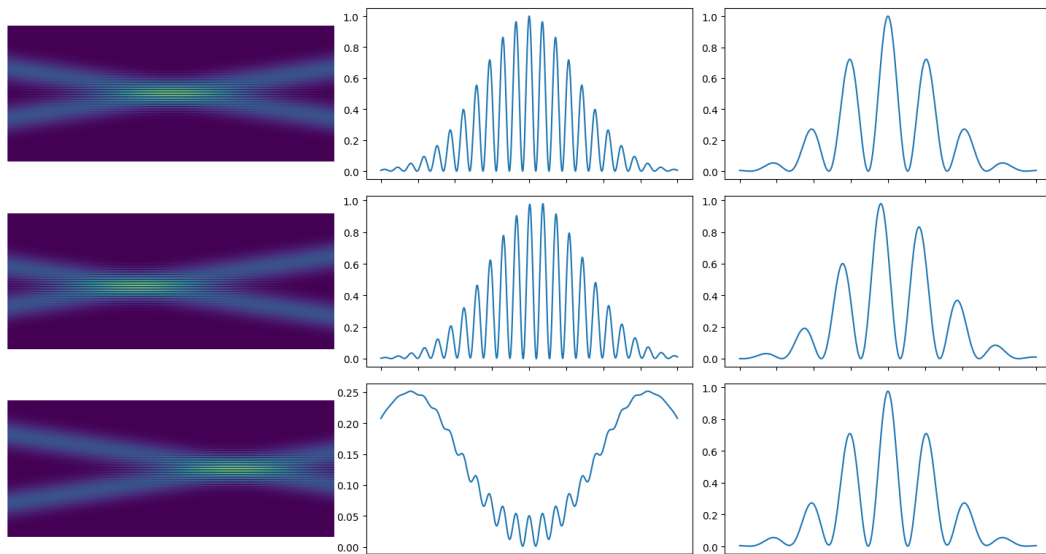


Figure 28: Simulation of different effects on the asymmetry. From left to right, the intersection of the beams and two pattern can be seen. The first corresponds to a stronger displacement and smaller lattice spacing than the second one. First row shows perfect alignment, the second displacement of one beam and the last of two beams by the same amount.

5.2 CONFINEMENT

The ultimate goal of a lattice is to confine atoms. As such a qualitative number for the degree of trapping is needed, given by the trap frequencies $(\omega_x, \omega_y, \omega_z)$, which can be found by approximating the interference fringes as harmonic potentials of the form:

$$V(\vec{x}) = \frac{m}{2}(\omega_x^2 x^2 + \omega_y^2 y^2 + \omega_z^2 z^2). \quad (19)$$

The resulting trap frequencies can be approximated as:

$$\omega_x = \sqrt{\frac{32aP}{\pi m w_x^3 w_z}}, \quad (20)$$

$$\omega_y \approx \sqrt{\frac{32aP}{\pi m w_x w_z} \cdot \frac{\sin^2(\theta)}{w_z^2}}, \quad (21)$$

$$\omega_z \approx \sqrt{\frac{16aP}{\pi m w_x w_z} \cdot \frac{\pi}{d}}. \quad (22)$$

where w_i is the waist of the beam, $a = \frac{3\pi c^3}{2\omega_0^3}(\frac{\Gamma}{\omega_0 - \omega_L} + \frac{\Gamma}{\omega_0 + \omega_L})$ and P the power in one beam. A detailed derivation of the trap frequencies can be found in [31]. From the trap frequencies in radial direction (x, y) one can read off the condition for isotropy by equalizing both formulas. This results in:

$$w_z = \sin(\theta)w_x. \quad (23)$$

Reaching the quasi-2D regime requires for one of the three trapping frequencies to strongly dominate over the other two. Thus populating only higher energy levels of two dimensions until a critical particle numbers N_{crit} is reached. Estimating the highest possible number of trapped particles with no excitation in the axial direction $n_z = 0$ can be done by looking at the energy spectrum of a harmonic oscillator. From the independence of the three spatial coordinates the total energy can be written as:

$$E_{\text{tot}} = \hbar\omega_x(n_x + \frac{1}{2}) + \hbar\omega_y(n_y + \frac{1}{2}) + \hbar\omega_z(n_z + \frac{1}{2}). \quad (24)$$

To freeze out excitations in z -direction the energy has to be lower than $\frac{3}{2}\hbar\omega_z$, leading to the inequality:

$$\omega_x(n_x + \frac{1}{2}) + \omega_y(n_y + \frac{1}{2}) < \omega_z. \quad (25)$$

From this the critical particle number per spin state can be read of as:

$$N_{\text{crit}} = \frac{1}{2}n_{x,\text{max}}n_{y,\text{max}} = \frac{\omega_z^2}{2\omega_x\omega_y}. \quad (26)$$

While this number is not exact as a result of approximations for example finite temperature or particle interactions, there is indeed a strong dependence on the aspect ratio [22]. And hence it can be interesting to be able to drive to larger aspect ratios to further probe the microscopic to mesoscopic transition in particle number.

5.3 OVERVIEW OF EXISTING ACCORDION LATTICES APPROACHES

In the following a brief overview of existing accordion lattice set-ups is given, to motivate the ideas of our set-up. This sections overview will be limited to setups which are eligible for our set-up.

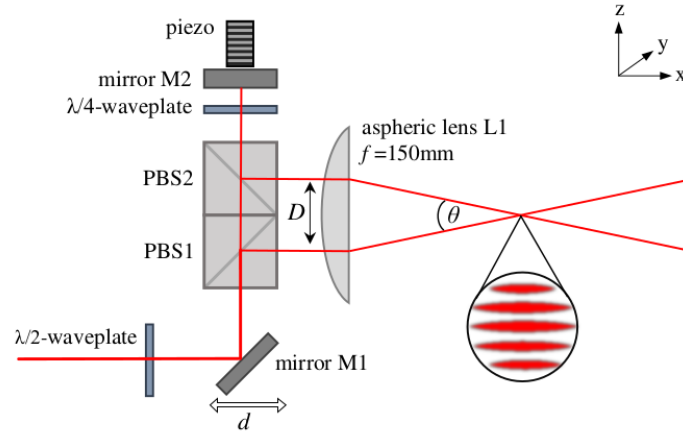


Figure 29: Accordion lattice with two PBSs. The beam translation is done by moving the mirror M1. The beam is splitted into two parallel ones via PBSs before being focused by a lens. Active phasestabilisation is done with a piezo-element situated behind mirror M2. Taken from [33].

The first possible approach comes originally from the Raizen group at the university of Texas in Austin [28]. The beam translation is realized with a mirror on a stage. To split the beam into parallel beams two PBSs are mounted on top of each other, see figure 29. Going through the first PBS the beam is splitted into a s-component going through the lens and a p-component going through both beamsplitters before being reflected by a mirror. Due to going through a $\lambda/4$ waveplate situated before the mirror twice the polarisation is shifted by π causing the beam to be reflected on the lens by the second beamsplitter. The first performance on atoms can be seen in Ville et al. [34].

A similar approach was taken by the Foot group [29] from the Clarendon Laboratory at the university of Oxford. With the difference that only one PBS is needed and that their set-up allows a two-dimensional accordion. For this a dual-axis Acousto Optical Deflector (AOD) is used and an optical set-up similar to a Michelson interferometer, see figure 30. The ingoing laser beam is separated by a PBS into two parts. One is reflected into itself with a mirror. The other shifted with a lens in front of a mirror. The parallel beams can then be focused with a AOD.

In both previously mentioned build-ups both beams undergo different paths. While the path length can be adjusted by the position of the mirror, any thermal fluctuation and therefore thermal expansion for example of the mirror changes the relative phase. To compensate this a piezoelement is mounted behind a mirror, actively compensating the change via a PID.

A different approach was taken by the Greiner group in Harvard (figure 31). Two dove prisms were glued together with a beamsplitter coating in between to split the beam into two parallel ones. Precise matching of the phase difference of both

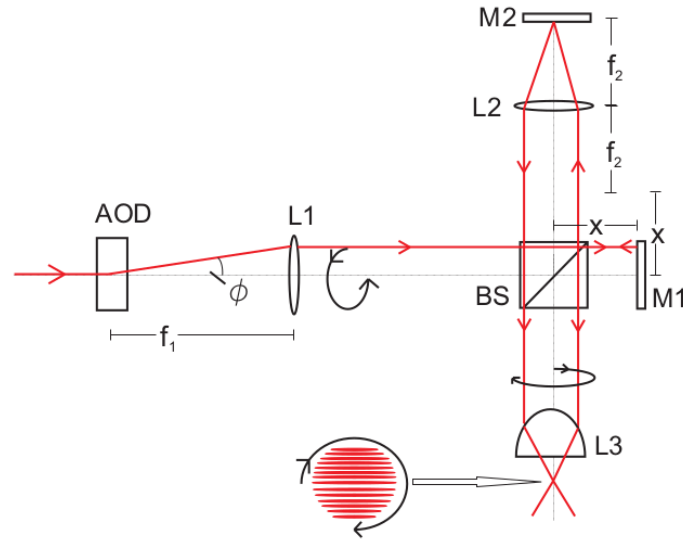


Figure 30: Accordion lattice with a single NPBS. BS is a non-polarising beam splitter cube, L_1 - L_3 are converging lenses and M_1 - M_2 are mirrors. The beam translation is done via an AOD. Taken from [29].

beams is done by matching interference pattern during glueing. Compared to the previous set-ups no PID to control the phase between the beams is needed here as the dove prims are monolithic.

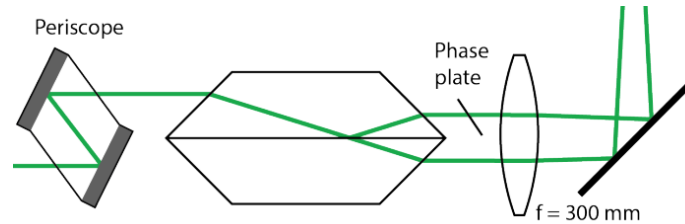


Figure 31: Accordion lattice consisting of two doveprims with beamsplitter coating in between. Taken from [32]

The different setups differ in the alignment precision and a summary in comparison to our implementation of an accordion lattice can be found in table 9.

5.4 NPBS AS WAY TO GO?

Most approaches mentioned previously require an additional stabilization of the pattern in form of a piezomirror controlled by a PID. Considering the underlying idea of HQA to use stable solutions whenever possible the Greiner method of glued dove prisms is the most suggestive choice. The glued dove prisms are ultimately a very precisely glued NPBS. Unclear is how far a commercially available NPBS can be used to obtain the accordion lattice. Especially in regards to parallelism of the beams since misalignment of the glued cube are apparent with the naked eye (see figure 32). Additionally to the visible misalignment of both triangles being translated to one another leading to a phase difference between the beams, there might be some angle or torsion happening leading to the beams to

come out under an angle.

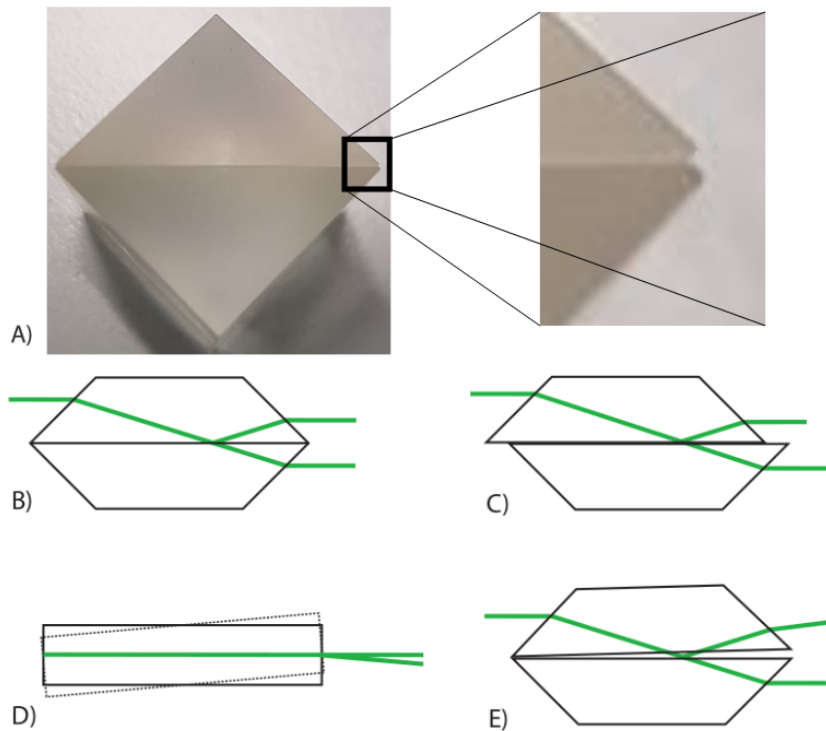


Figure 32: Possible misalignments NPBS. In A) a picture of a NPBS can be seen. The zoom of the edges shows the chamfer cut as well as a translation of the individual triangles to one another. B) shows the optimal setting. In C) a translation along the glued plane can be seen, leading to a phase difference between both beams. D) and E) show misalignments leading to the beams not being parallel. Taken in parts from [32].

Compared to the previously mentioned realizations of an accordion lattice, our setup intends to use an microscope objective (Mitutoyo G Plan Apo 20X) instead of a single lens to focus the parallel beams together. Since this high NA objective has a small aperture the maximum beam separation is also 5.6 mm. Therefore a 12.7 mm NPBS is sufficient to drive the beam separation.

The percentage of transmitted light through the Mitutoyo objective is dependent on the wavelength, see figure 33. For a transmission around 90% the wavelength has to be between 500 – 700 nm, thus setting the possible wavelengths for the accordion lattice.

5.5 BEAM TRANSLATION

To drive the beam separation a translation of the ingoing beam is needed. This needs to be done in a way which does not change the parallelism of the beams. There are several possible ways to do this, either with a linear stage, two parallel beams/galvanometer or an AOD.

Commerical linear translation stages allow velocities of the order of 500 mm/s leading to a quench time to drive from maximum to minimum spacing of ~ 10 ms, for our settings. The time scale might even be higher taking the acceleration and de-

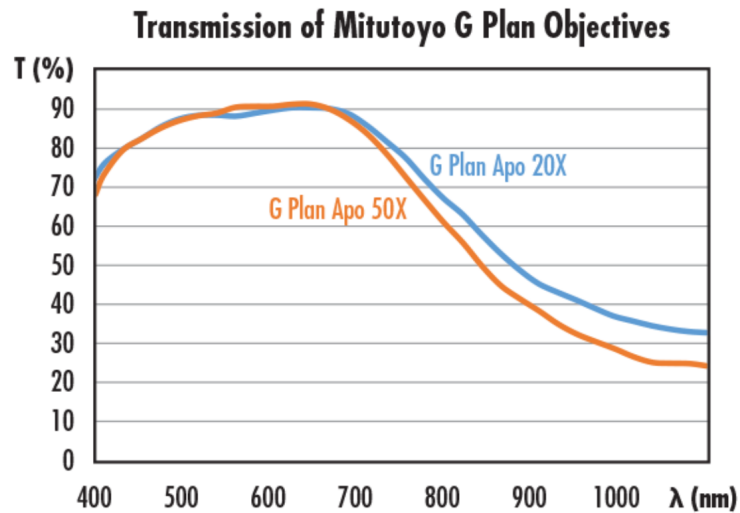


Figure 33: Percentage of transmitted light in dependence of the wavelength for the Mitutoyo G Plan Apo 20X and G Plan Apo 50X.

celeration into account. Since this might limit potential future quench experiments other possibilities are considered. While a galvanometer can be considerably faster, by an order of 10 [32, 35], induced vibrations may lead to shifts of the central fringe [28].

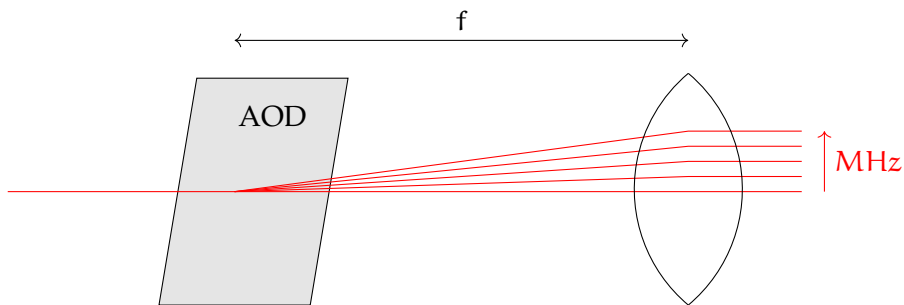


Figure 34: Setup of how an AOD beam angle can be translated into parallel beam displacements

Given these points an AOD was selected for the beam translation, with driving times on the order of μs . An AOD compared to an AOM is optimized for large deflection angles and uniform diffraction efficiency within their bandwidth. To translate the diffracted beams of the AOD to parallel beams, a lens is used as can be seen in figure 34. Going through the AOD there are two options, either using a focused beam or a collimated one. While a focused beam leads to faster switching times as well as being focused on the atoms, using a few Watts of laser intensity might lead to damage as the maximal damage threshold is commonly around 5 W/mm^2 for 532 nm. Another reason is that for reaching large lattice spacing, on the order of $15\text{ }\mu\text{m}$, small beam separations, on the order of $400\text{ }\mu\text{m}$, are necessary. Leading to small beam waists being necessary at the edges of the NPBS cube to avoid clipping.

One option would be to use collimated beams and to build a telescope behind the NPBS. The issue here is that optimally aspherical lens should be used as spherical aberrations cause among other shift of the intersection point for different spacings [33–35]. Additionally this would decrease the number of points of resolution (section 5.6). Another possibility is to use focused beams through the NPBS e.g. collimated beams on the atoms and AOD. Here one has to be cautious of where the focus should lie as well as of the damage threshold of the glass cell, see section 5.6. The choice was in favour of having the focus close to the NPBS and being collimated at the AOD.

A possible AOD for this undertaking is the DTSX-400 from A&A Optoelectronics. The selection was done according to previous works [29, 36]. With a scan angle of 41 mrad@532 nm a lens with focal length of 75 mm leads to the wanted displacement on the order of 3 mm. While larger focal length enables a larger displacement they limit the possible waist on the atoms, as will be discussed below.

AOD	Resolution (N)	Rise time	Active aperture	Scan angle
DTSX-400	500 dots	1 $\mu\text{m}/\text{s}$	7.5 mm x 7.5 mm	41 mrad@532 nm

Table 7: Parameters of AOD DTSX-400

An additional remark to take into account is that changing the frequency of the AOD gives rise to a change of intensity in the first order diffraction. The diffraction efficiency for DTSX-400 for example is >70%. This needs to be compensated by controlling the rf power fed into the AOD. It can be done with a lookup table.

5.6 PARAMETERS OF THE PLANNED SETUP

In section 5.4, the general idea of HQAs envisioned optical accordion has been outlined. The open parameters left are λ the wavelength of the laser beam, P its power and the beam waists on the atoms. Their values or rather the range of possible values are influenced by different boundaries explained in this section.

Depending on the chosen wavelength either a blue or a red detuned trap is possible. In case of a blue detuned trap the wavelength is below resonance (<671 nm) and the intensity maximum corresponds with a potential minimum. Red detuning corresponds accordingly to a wavelength above resonance (>671 nm) and the potential minimum is situated at the intensity minimum. As the objective sets the wavelength range to 500 – 700 nm, both detunings are possible. The following calculations are therefore made with 532 nm for the blue detuned side. A wavelength of 532 nm is a conveniently available from frequency doubling 1064 nm laser light. For the red detuned side 680 nm was chosen as it is in the transmission range of the Mitutoyo, but in principle further detuned wavelength are also a possibility at the cost of lower transmission.

To be collimated on the atoms a Rayleigh length $z_R = \frac{\pi w_0^2}{\lambda}$ of at least twice the working distance, 30.6 mm, of the objective is planned. This sets the lower bound of possible waists to 100 μm and 120 μm for 532 nm and 680 nm respectively. The upper bound is determined by two parameters of the AOD. First, the active aperture of the AOD, since the lens behind the AOD forms a telescope with the objective. The demagnification between AOD and atom plane is 7.5 as the effective focal lens of the Mitutoyo is 10 mm. Therefore the active aperture of 7.5 mm sets the

upper bound for the waist to 1 mm. Second, the resolution of the AOD setting the number of spots that can be resolved on the atoms [32]. The resolution is given by [37]

$$N = \frac{\Delta\theta}{\Delta\Theta} = \frac{\Delta\theta \cdot D}{\lambda}. \quad (27)$$

the number of angles θ that can be addressed, in units of the beam divergence angle Θ . For a collimated Gaussian beam the divergence angle is given by its width D and the wavelength λ . To reach the maximal resolution the beam should fill out the aperture of the AOD, this can be adjusted by adapting the lens behind the AOD and thus changing the telescope. To estimate the required resolution the waist perpendicular to the fringes w_p and the minimal spacing s_{\min} is needed. Since the resolution points N can be written as [32]

$$N \approx \frac{w_p}{s_{\min}}. \quad (28)$$

From the resolution in table 7 and the minimal spacing the upper bound of the waist can be found

$$w_p = N \cdot s_{\min} \approx \begin{cases} 500\mu\text{m} & 532 \text{ nm} \\ 600\mu\text{m} & 680 \text{ nm} \end{cases} \quad (29)$$

Finally an isotropic confinement for the smallest spacing is pursued for uniform expansions. This sets the relation between the waists to

$$w_z = \sin(\theta)w_x = 0.28w_x \quad (30)$$

given by the NA of the objective.

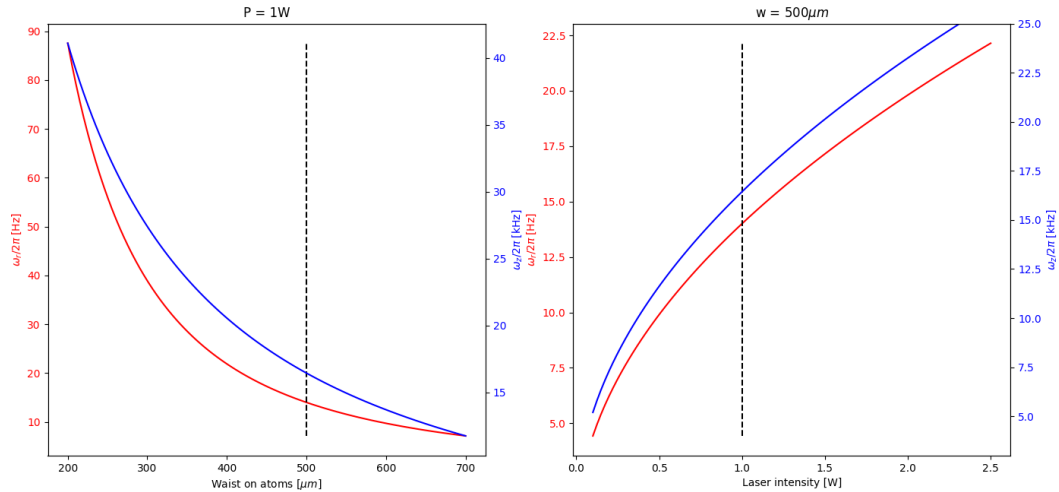


Figure 35: Calculated trapping frequencies in axial and radial direction for 532 nm. The waist w_z is chosen such that the axial frequencies is equal for the lowest spacing. On the right the dependents on the waist can be seen and on the left the dependents on the power. The dotted lines correspond to the chosen parameter for the respective other picture.

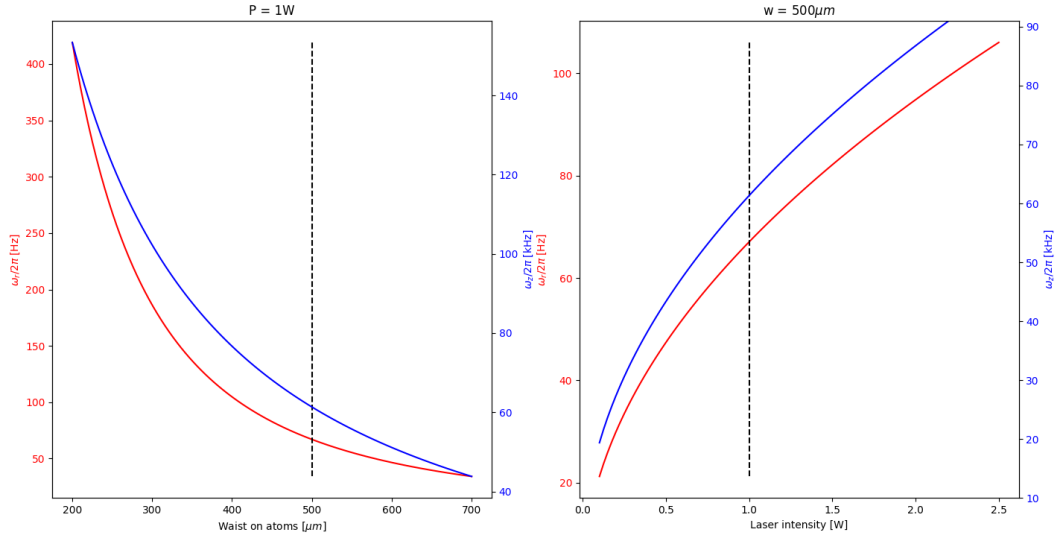


Figure 36: Calculated trapping frequencies in axial and radial direction for 680 nm. The waist w_z is chosen such that the axial frequencies is equal for the lowest spacing. On the right the dependents on the waist can be seen and on the left the dependents on the power. The dotted lines correspond to the chosen parameter for the respective other picture.

The optimal waist parameters are dependent on the preferred trap frequencies. For the purpose of quantitative investigation of the 2D spilling the axial trap frequency range should include both values of the already standing experiments, see table 6. The spacing of this accordion setup can be altered by a factor ~ 15 (see 5.7.2) leading to a factor of $1/15$ in axial trap frequencies. Thus the dynamic range of the accordion allows to change between both experiments settings as long as the maximal ω_z is between $2\pi \cdot (29 - 105)\text{kHz}$. For the radial confinement lower values are beneficial for overlaying the magnetic field. Here frequencies in the range of 60 Hz or lower are envisioned.

Finally the laser intensity needs to be less than the damage threshold of the glass cell. The dependence of the trap frequencies on the waist and laser intensity for both wavelength are plotted in figure 35 and 36. Possible configurations are summarized in the table below.

λ [nm]	min waist [μm]	max waist [μm]	w_x [μm]	w_z [μm]	ω_x [Hz]	ω_z [Hz]	P [W]	I [W cm $^{-2}$]
532	120	500	500	140	20	24	2	900
680	100	600	500	140	36	34	0.3	140

Table 8: One possible set of parameters for both wavelength.

The final settings need to be decided after a more thorough market research about possible AOD and available NPBS.

5.7 EXPERIMENTAL SETUP

As a first try an 80 MHz-AOM and a lens with 200 mm focal lens was used. This leads to a beam translation range of approximately 3 mm. Furthermore 671 nm laser light was used due to its availability. In figure 37 one can see an overview of the experimental setup of the accordion lattice. Note the $\lambda/2$ waveplate in front of the NPBS, which is needed to ensure that both beams after the NPBS have an approximately even splitting. While the NPBS has no dependency of the splitting ratio on the polarisation in case of using it at 90 degree, there is a significant dependency on the polarisation in case of 45 degree. The case of uneven power splitting was discussed in section 5.1 and can be seen in figure 26. Behind the NPBS an additional PBS is mounted to further improve the contrast associated to the polarisation.

Since the trap is in the blue detuned regime with 532 nm, there needs to be a minimum to trap the atoms, with the current setup the central fringe is a maximum which means an additional π -shift of one of the beams is needed. This can be done by inserting a π phase plate behind the NPBS to one of the beams.

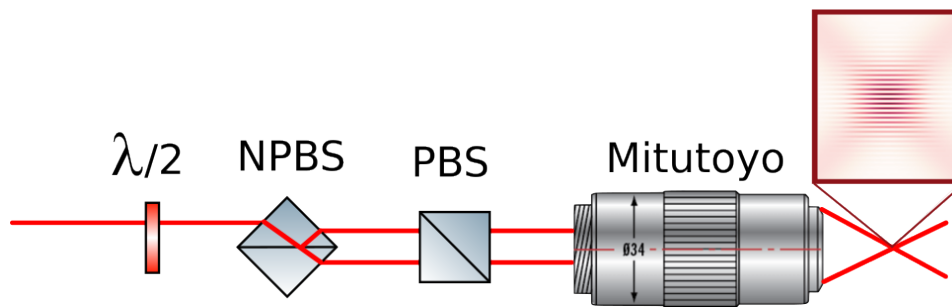


Figure 37: Schematic of the accordion setup. A $\lambda/2$ waveplate for the power splitting, a NPBS for the beam splitting, a PBS to clean the polarisation and finally the Mitutoyo objective to intersect the beams.

5.7.1 Alignment

To align the lens after the AOD it is mounted on a translation stage. The beam is aligned such that the central frequency hits the lens in the centre. Coarse alignment is done by sweeping between two frequencies at a rate of the order of 100 Hz such that it seems for the human eye as if both beams are there at the same time. If the lens is at the right position both beams are parallel to each other. In case that the beams are converging the lens is too close to the AOD and in case of divergence it's the other way around. The beams were aligned to < 0.17 mrad precision with the Shack-Hartmann sensor (WFS150-SC). The sensor was positioned such that for several frequencies the angle of the beam to the sensor can be measured. Limited by the size of the sensor only a range of ~ 20 MHz $\hat{=}$ ~ 0.7 mm is measurable without displacing the sensor.

The beams after the NPBS need to be parallel to each other for all beam separations. This can be tuned by precise placement of the laser path as well as the adjusting the angles of the NPBS. The coarse alignment is done by aligning the laser beam to the hole row and placing the NPBS such that the beams appear to be parallel

with the bare eye for the smallest and largest displacement. Additionally one has to verify that the driven separation corresponds to the desired range of $\sim 300 \mu\text{m}$ to $\sim 5 \text{ mm}$.

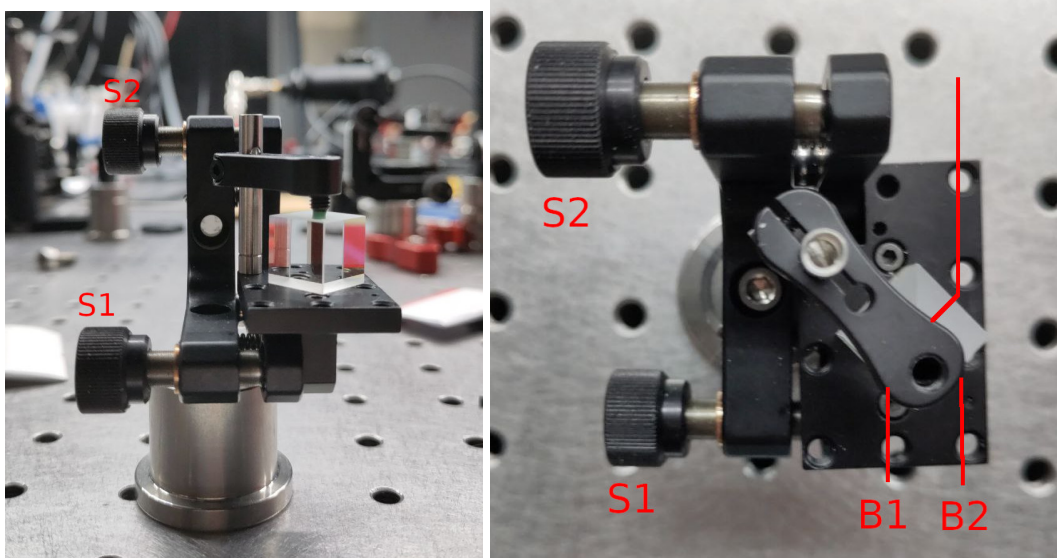


Figure 38: Mounting of the NPBS. Two DOFs for the tilt and rotation of the NPBS to assure parallelism between the incident light and splitting plane.

The NPBS is mounted on a two axis mount allowing a tilt along the y-axis and a rotation along the z-axis. In figure 38 the mounting is depicted, for convenience the screws and the reflected and translated beams are given names. It is convenient to first coarse align the y-axis using the S2 screw such that both beams y-positions don't deviate more than $50 \mu\text{m}$. Afterwards it is reasonable to check again that the beams are coarsely parallel as well as the correct separation range. What is left is to parallelise the beams to a better precision. This can be done by measuring with a beam profiler the separation of the beam centres at different position e.g. as far as possible away.

For fine alignment it is important to know what impact each screw has on the setup:

- screw S1:
 - Beam B1: x- position changes, y-position remains approx. same
 - Beam B2: remains approx. same
- screw S2:
 - Beam B1: x- position changes, y-position changes
 - Beam B2: x- position remains approx. same, y-position changes

Now the way to go is to use screw S1 to fix the parallelism in x-direction. Then beam walk with both screws to leave the x-position untouched while fixing the y alignment. This might take a few iterations to align.

The results can be seen in figure 39 and figure 40. Figure 39 shows the parallelism of the beams in mrad. The beams were measured at 30 cm distance and the error arises from the Gaussian fit of the beam profiler. In the centre region of the AOM

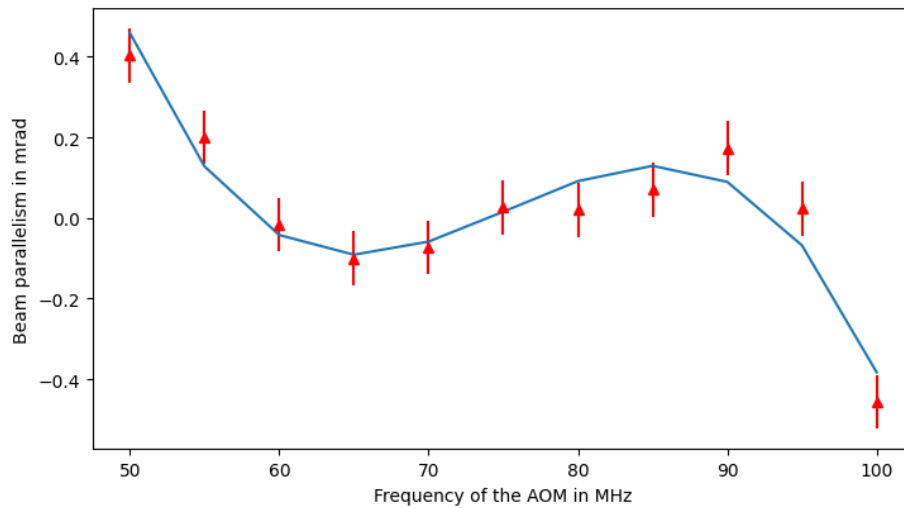


Figure 39: Parallelism of the beams in dependence on the frequency of the AOD. The visible 3-order polynomial is only a guide to the eye.

(80 MHz) the beams deviate only by 0.2 mrad. Further from the centre larger deviations can be seen. A 3-order polynomial was fitted as a guide to the eye. Most likely the apparent divergence or respective convergence for higher and lower frequencies stems from the 200 mm planoconvex lens in the the backfocal plan of the AOM. Here a aspherical lens might fix the issue. If the lens was simply at the wrong position one would expect a divergence or convergence for all frequencies. The beam steering should be apparent already directly after the AOM but was not noticed since the Shack-Hartmann sensor only allows to measure a small frequency region in this case of 65 MHz to 85 MHz.

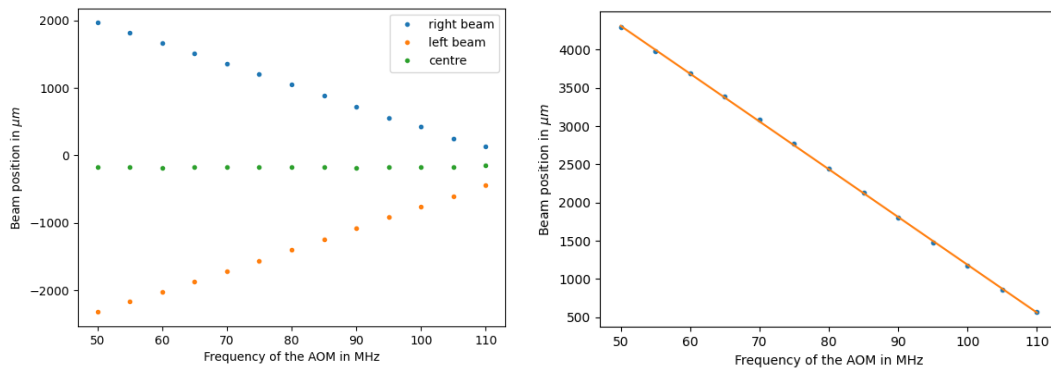


Figure 40: Spacing of the beams after the NPBS. On the right the position of the individual beams is plotted for different frequencies as well as the centre position. The offset of the centre position is arbitrary given by the placing of the beam profiler. On the left the beam separation over the frequency of the AOM can be seen.

The beam spacing for different frequencies can be seen in figure 40. Here two things can be seen, first the position of the right and left beam showing that the translation happens equally in both beams and that the centre shifts within 1σ .

One can also see the total beam separation over the applied frequency. The fit gives a slope of:

$$(-62.51 \pm 0.05)\mu\text{m}/\text{MHz} \quad (31)$$

The final step is to align the Mitutoyo objective. Here it is important that the beams hit the aperture perpendicularly. A tilt of the aperture leads to a shift of the intersection point relative to the focal point as well as a movement of the central fringe during compression. Therefore a tilt of the Mitutoyo relative to the beams needs to be decreased as far as possible. One way to go is to ensure that the beams reflected on the aperture overlap with the ingoing beams. Since the reflection of the beams on the aperture is not visible, a mirror was mounted/clamped on the Mitutoyo.

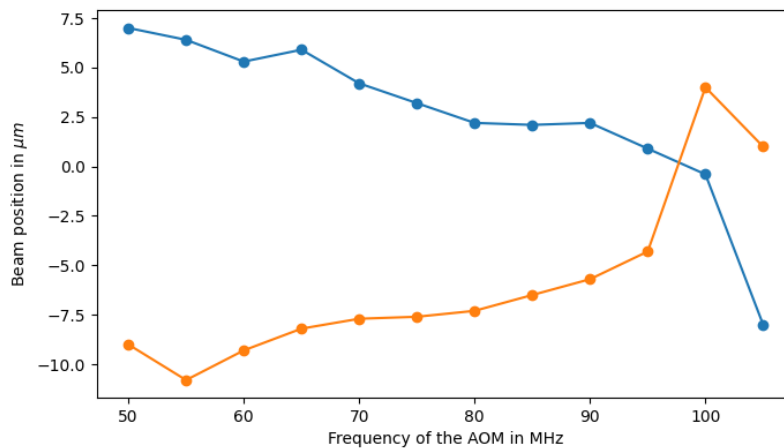


Figure 41: Shift of beams in focal point during compression in x direction. The lines in between the data points serve as a guide to the eye.

As variation of the trap depth leads to unwanted heating, it is necessary to reduce possible occurrences. One possible source of heating is the varying overlap of the beams during compression [34]. The movement of the individual beams in the focal point can be seen in figure 41. These were measured by placing a camera in the focal point and measuring the beam position for different frequencies. The other beam needs to be blocked such that no interference pattern obscures the measurement. Each beam moves a bit less than $20\mu\text{m}$, which is the same order of magnitude as other works [33–35] and well within our designated waist of $\sim 100\mu\text{m}$. For the y direction similar numbers were obtained. Therefore the beams always overlapped during compression.

5.7.2 Measurement

In figure 42 one can see the pattern of the lattice without a PBS. A PBS placed behind the NPBS ensures a clean polarisation after the beamsplitting. The shape is as described in the theory (section 5.1). The contrast between a minimum and a maximum in the middle is weaker than expected, with a contrast ~ 0.8 .

The power of both beams was balanced to $\sim 49 : 51$ with a $\lambda/2$ -waveplate in front of

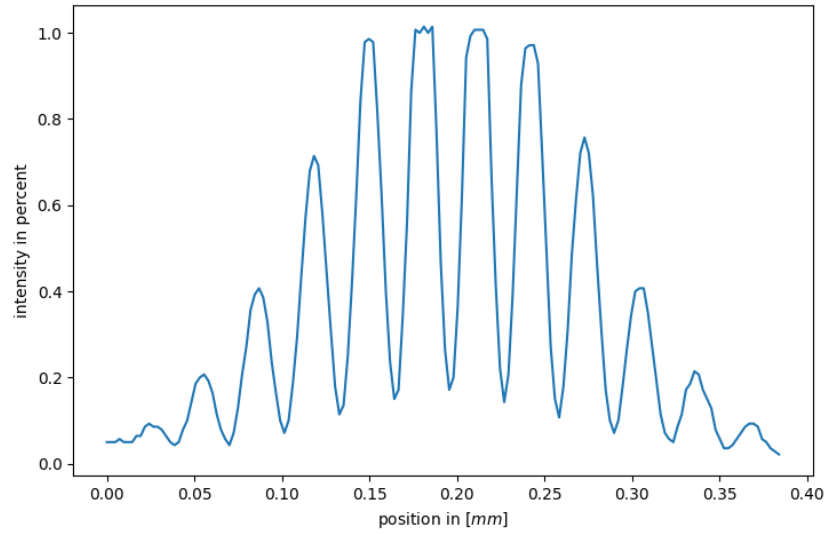


Figure 42: Picture of the lattice measured with a microscope objective without PBS to clean the polarisation.

the NPBS. From the comparison to figure 27 one can conclude, that the polarisation between the two beams doesn't match perfectly. The NPBS has a specification of less than 10% of the polarisation in the wrong axis. Compared to the figures in the simulation the contrast seems to correspond rather to $\sim 20\%$ of the polarisation in the wrong axis. The enlarged mismatch of the polarisation can stem from the fact that we are not going in a 90° angle to the surface but rather a 45° angle. To ensure that the polarisation is parallel to the layers a PBS is used.

An exemplary picture of the lattice pattern with PBS can be seen in figure 43. Here the contrast is significantly better (~ 0.95). To get the spacing and compare it with the theory, a cut of the lattice pattern along the x-axis is made. Here a fit can be applied to get the relevant parameters. The fit function used is:

$$\exp(-(x-d)^2/c) \cdot (A + 2B \cdot \cos(2\pi/f \cdot (x-d) + g)) \quad (32)$$

in accordance with the theory. Here d describes the centre position of the Gaussian envelope and c its width. The amplitudes are given by A and B . In the following sections the main focus lies on the parameter f which describes the spacing of the lattice and g which gives the phase. The convergence of the fit is highly dependent on the start parameters especially on the spacing. As such a first guess is given by the spacing of the relative maximums.

In figure 44 the theoretical values of the spacing are plotted additionally to the measured ones. For the theoretical calculations equation 11 was used as well as the approximation $\sin(\theta) = \frac{D}{2f}$ with D the aperture of the focusing lens/objective and f its focal length.

The measured spacings is in good agreement with the theoretical estimation.

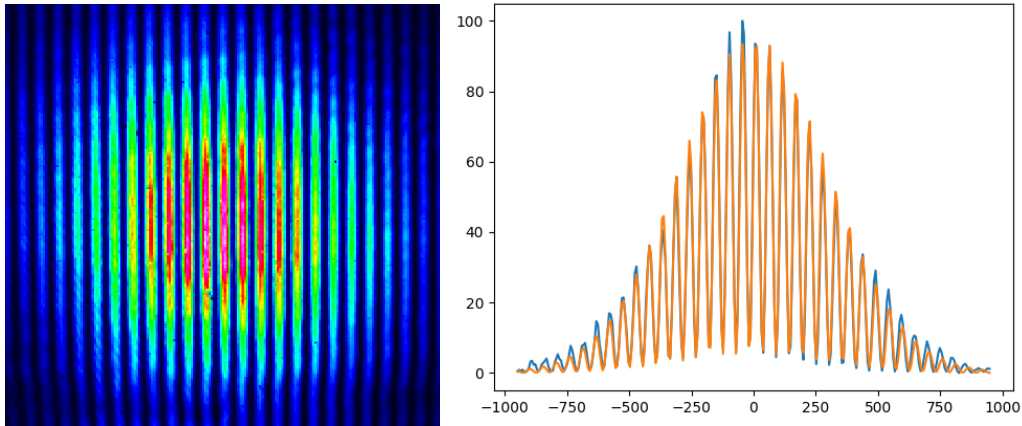


Figure 43: Image of the lattice interference pattern taken with a microscope objective and beam profiler. The plot on the right shows a cut through the image along the x axis and the corresponding fit.

5.7.3 Stability

The movement of the central fringe over time and during compression is crucial for the implementation of the accordion lattice. Displacements leading to unwanted heating and potential shifts out of focus of the imaging objective. Therefore the camera was positioned at a fixed point and pictures of the lattice for different spacings were taken. Concatenating these to a joint figure gives an overview over the dynamic stability of the fringes and can be seen in figure 45 and 46. As a guide to the eye the central fringe position is marked. Both pictures were done with different NPBS and set-ups. The set-up for figure 45 had a linear stage as tool for the beam displacement, while the displacement in figure 46 was done with an AOM. The lattice spacing range for the linear stage from 1.2 to 6 μm and for the AOM from ~ 1.5 to 12 μm . Instead of collimated beam the AOM setup uses a focused beam close to the NPBS allow for larger lattice spacing since smaller beam separations are possible.

For the linear stage the central fringe movement is around 0.8 μm , while the displacement for the AOM is of the order of 1.9 μm . This stems from the larger lattice spacing range but might come from the fact, that the beams do not remain parallel for large beam separation as can be seen in figure 39. If restricted to the same lattice spacing range the centre movement is 0.8 μm compared to 1.9 μm . It is likely that either the NPBSs are that different or the lens behind the AOM is that crucial. To be sure the measurement should be redone with preferably an aspherical lens behind the AOD. The depth of focus of the imaging objective is ~ 1 μm depending on wavelength [6]. Such that the current measured dynamic range leads to the central fringe being out of focus during the compression. If using different cubes and the right lens does not fix this, then one could think of actively shifting the central fringe for example by using a phase plate for one of the beams.

From figure 46 one can also see the intensity fluctuations of the central fringe. One reason for them is the deflection efficiency of the AOD which has to be adjusted by the ingoing rf power. Another reason is the asymmetry of the pattern caused by the movement of the intersection point. This causes changes of intensities on the order of $<5\%$. These can also be adjusted by the rf power. The estimation

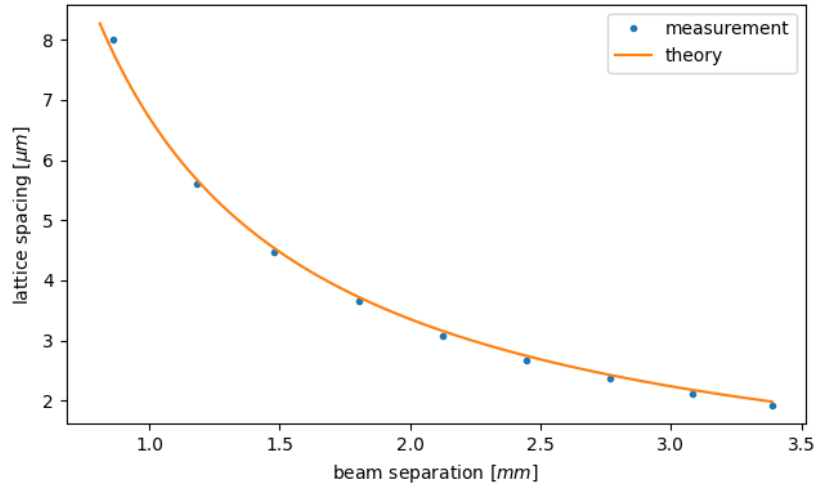


Figure 44: Lattice spacing in dependence of the beam separation. The orange line visualizes the theoretical expectation, the blue dots the measurement.

comes from measuring the laser intensity behind the [AOD](#) and comparing it with the central fringe power.

The position of the zeros order maximums changes, because the phase between the two beams is shifted. Possible phase shifts arise from the path difference L or the wavelength λ :

$$\Phi = \frac{2\pi L}{\lambda} \quad (33)$$

The measurement was done with a locked laser, such that the frequency can be seen as constant. Therefore a change of the path difference L is more likely. Possible reasons for a path difference are tilts for example of the Mitutoyo objective or microscope objective or the apparent misglue of the [NPBS](#).

Another aspect of the stability is the temporal continuity. The temporal stability is measured by recording the position of the central fringe while keeping the camera fixed. The power in the accordion port for this measurement was 1 mW for the first 40 hours. By removing a neutral density filter in front of the fiber port the power was than doubled for the remaining time. The results can be seen in figure [47](#), the measurement was done with the linear stage setup.

After a steep increase for the first 10 hours, the phase of the interference fringes is constantly increasing with a lower slope. The system has not settled even after nearly 5 days. To find the cause some numbers are estimated. Assuming a constant wavelength the path difference has to change according to:

$$\Delta\Phi = \Phi_1 - \Phi_0 = \frac{2\pi\Delta L}{\lambda} \quad (34)$$

For $\Delta\Phi \approx 2\pi \cdot 0.07$ this leads to $\Delta L \approx 47$ nm. With a thermal coefficient of $5.5 \cdot 10^{-7} \frac{1}{\text{K}}$ for fused silica and an estimate of the path difference of less than 1 mm, thickness of cementing and shear translation of the cube, the path difference changes with 0.55 nm/K. Therefore the phase can't stem from a temperature change, for example of the laboratory or for the laser power. Especially since the phase

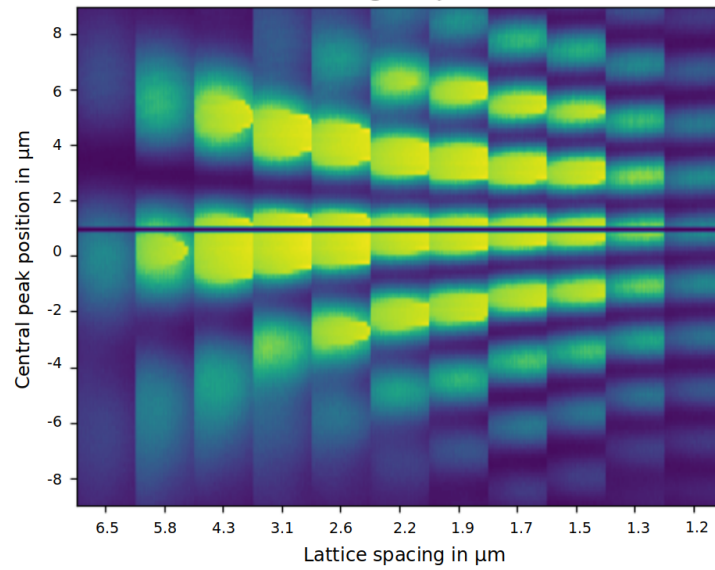


Figure 45: Dynamic stability of the lattice for the linear stage approach. The line serves as a guide to the eye.

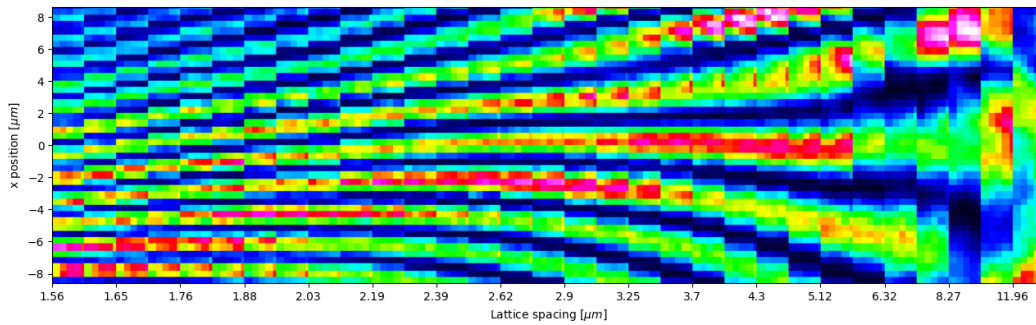


Figure 46: Dynamic stability of the lattice for the AOM. The distortion starting 6 μm stems from the chamfer cut.

drift doesn't increase after doubling the power. The most likely guess would be a slack of the optical components, especially as the phase is deviating only in one direction, making vibrations or air fluctuations unlikely. Further the envelope of the Gaussian beam was studied over time resulting in a drift of $\sim 0.5 \mu\text{m}$. Making it probable that slack is happening.

One of the central advantage of this accordion lattice is the redundancy of phase stabilisation. This only holds if the phase stabilises over time to a constant value. Over the measured time this was not the case. For setups inspired by the Raizen group a drift of more than π within 6 hours is being measured [33, 35] and even in case of phase stabilisation with a PID it drifts around $0.05 \cdot 2\pi$ [33] which is equal to our drift within 5 days.

To understand the phase drift further measurements need to be done, for example with the AOD setup. For the future this setup is intended as a module, where it is expected to be more passively stable.

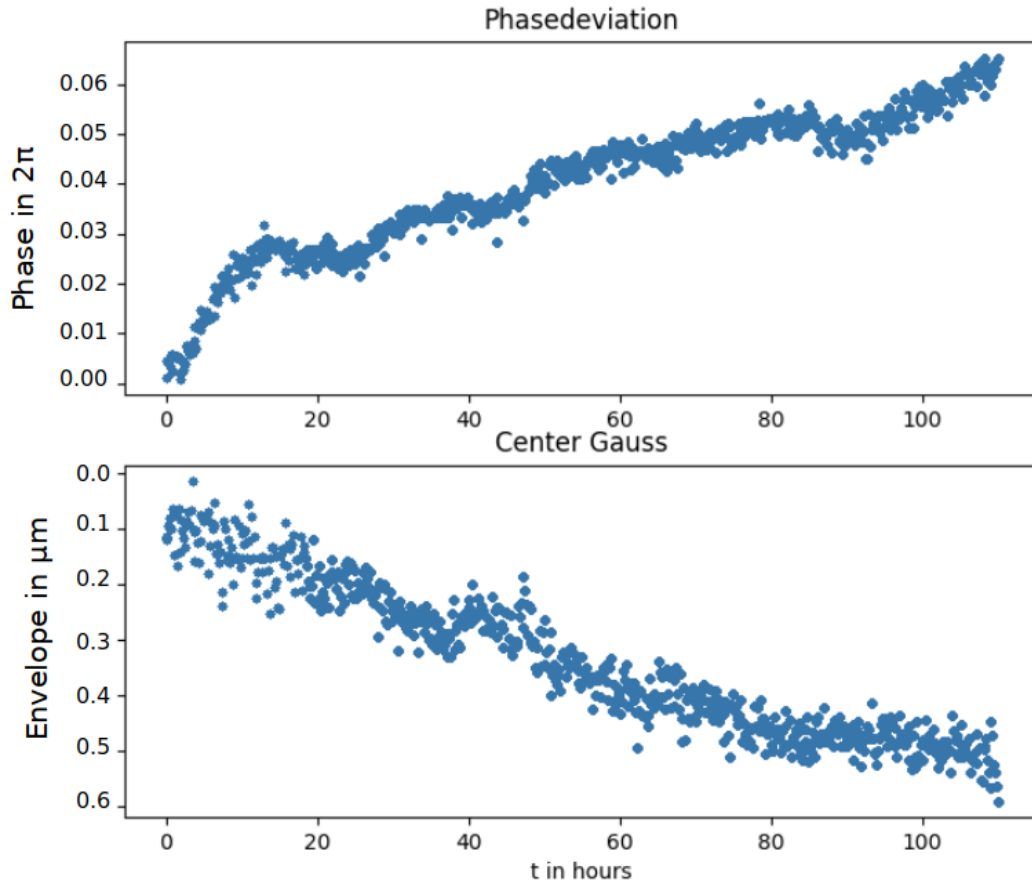


Figure 47: Temporal stability of the lattice. The upper figure shows the phase of the lattice while the lower figure shows the centre position of the Gaussian envelope.

5.7.4 Limitations and choosing the right components

Commercially available [NPBS](#) are not designed for an incidence angle of 45° . For example the AR coating is not such angles leading to a reflection of up to 30% of the incoming light. This can be fixed by a custom cube with the right coating. Additionally the chamfercut of the edges of the [NPBS](#) might induce some distortion for small beam separations. Beams are affected by the chamfercut for spacing smaller than $700\ \mu\text{m}$. While such an effect is not visible in the parallelism of the beams for different spacings see [figure 39](#), possible distortions of the wavefront may happen. In [figure 48](#) one can see the lattice for beams going through the chamfercut. While the fringes in x direction remain a distortion in y direction can be seen.

Both right angle prisms are cemented together. This means that a thin layer is between the prisms, which may cause an additional phase shift between the beams or in case of an uneven distribution misalignments as seen in [figure 32](#). From the measurement no indication of this was found.

A partially open question is how precise the glueing of the cube needs to be for our case. The current commercial cube is comparable in the central fringe movement to other build set-ups but considerably less precise than the precision glueing. A comparison between different realisations are summarized in [table 9](#).

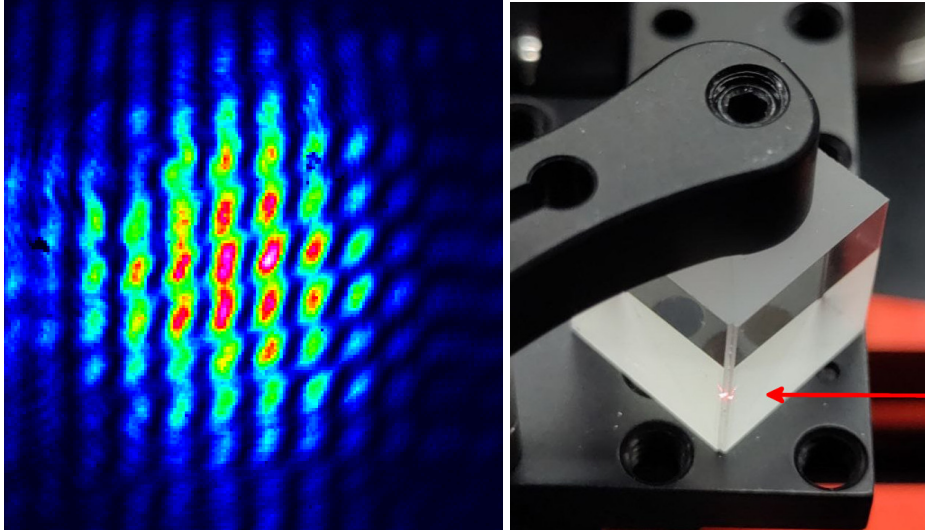


Figure 48: The left image shows the interference pattern for beams at the chamfercut. The right picture shows the beams at the chamfercut.

Group	spacing	beam pos. focus	central fringe pos.
Raizen [28]	0.96 – 11.2 μm	-	<2.7 μm
Dalibard [34]	2 – 11 μm	$\sim 20 \mu\text{m}$	-
Pfau [33]	3.5 – 35 μm	-	9 μm
Ferlaino [35]	2.5 – 11.2 μm	$\sim 20 \mu\text{m}$	1.6 μm
Greiner [32]	0.26 – (5 – 10) μm	-	<0.3 λ
NPBS	$\sim 1 – 15 \mu\text{m}$	$\sim 20 \mu\text{m}$	1.9 μm

Table 9: Different accordion lattice approaches and their precision.

While the movement is comparable to other setups, it is larger than the depth of focus, leading to the central fringe to be out of focus.

5.8 TOWARDS A MODULE

As all components around the glass cell, the accordion lattice is planned as a module. The current status is more of a proof of principle for using a NPBS as an accordion lattice than a finalised setup. This section will outline the conceptual ideas of the planned module.

For the module the degrees of freedom are reduced to only the necessary ones, making it easier to align while maintaining the same precision. The remaining degrees of freedom are summarized in the following:

- 4 DOF for hitting the glass cell and atoms perpendicularly
- 1 DOF placing the NPBS in the right range
- 2 DOF angles of NPBS
- 2 DOF Mitutoyo (+ 1 placing)

- 1 DOF position lens after AOD

To understand the necessity of the degree of freedoms, the individual components will be revisited with respect to the precision needed for alignment. For the module to be exchangeable, i.e. allowing to remove and add the module at different ports, without excessive realignment a short fiber is planned to be permanently attached to the fiber outcoupler. As plugging in and out of the fiber leads to a beam steering even when using the same fiber. Numbers for the deviation can be found in detail in [27], in case of the same fiber the standard deviation amounts to approximately 0.22 mrad.

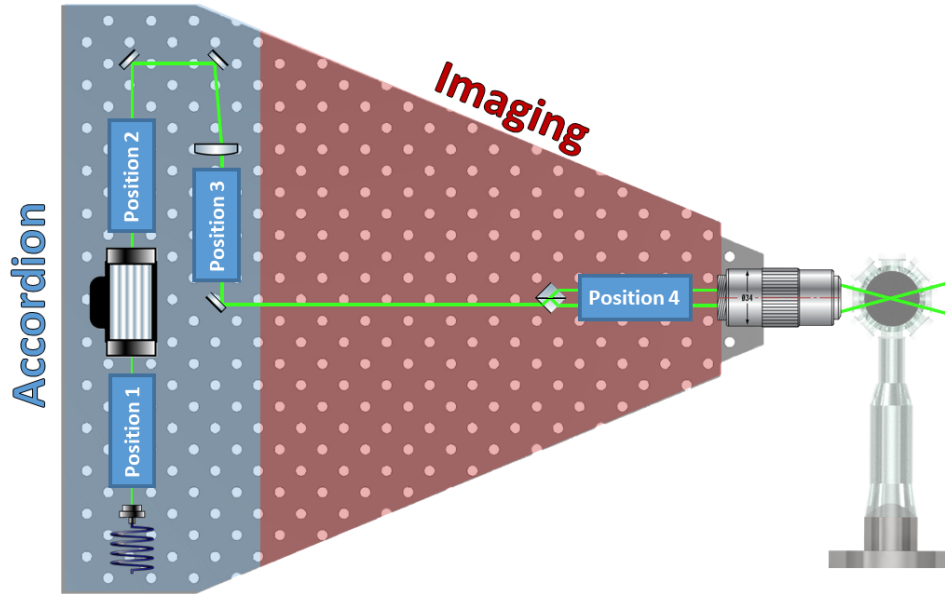


Figure 49: Sketch of the planned accordion module. The laser light comes from a fiber in the bottom left. Along the optical path are an AOD, a lens, a NPBS and the Mitutoyo objective. In between the single components, space for different optical components is given. Additionally in red space for imaging is highlighted. This is made accessible by for example placing a dichroic cube between the NPBS and Mitutoyo. On the right the glass cell can be seen.

The placement of the AOD is not critical and is best done in a similar way as in the doublepassmodule [25]. As the layers are perpendicular to the z direction, the beams also require a beam translation within z direction. Therefore the mounting of the AOD needs to be turned by 90° .

Behind the AOD the lens for the beamtranslation is situated, a precise positioning of this lens is important as it is of relevance that the displaced beams are parallel to each other. How precise the positioning needs to be, in mrad is not certain, as it is also unclear if the movement of the central fringe in figure 46 stems from the parallelism of the beams or from the glueing of the cube itself.

The distance between the lens and the Mitutoyo is fixed as they form a telescope. Additionally the position of the Mitutoyo is predetermined with respect to the glass cell, given by the working distance. As such it might be more convenient to build the module starting with the Mitutoyo, then place the lens at the right distance and afterwards the AOD. Or allow a slight adjustment between the lens and the Mitutoyo by adjusted placements of for example mirrors.

Before placing the **NPBS** a coarse alignment of the beam to the atoms should be done, this means ensuring that the beam hits the atom cloud and is perpendicular to the glass cell viewport. Fine alignment needs to be done later by adjusting the placement of the central fringe to be within the depth of focus of the imaging objective. This can only be done behind the **NPBS** as movements of the beam before the **NPBS** make the alignment of the cube redundant.

The placement of the **NPBS** only slightly changes the beams as the midpoint between the beams remains practically unchanged during compression and similar to the initial beam, see figure 40, leaving the coarse alignment nearly unchanged. Important for the placement is that the correct range of beam separation is selected. A description how to do so and an explanation of the two DOFs for the tilting can be found in section 5.7.1. As for the **AOD**, the setup needs to be turned 90° and therefore the mount needs to be adapted.

The Mitutoyo allows no degree of freedom to actively align to the atoms. The placement is predetermined by the position of the atom cloud and the tilt is determined by the parallel beams going onto the aperture. Therefore the sole possibilities without changing the **NPBS** to align the central fringe to the depth of focus are either by a changing the phase of one of the beams with respect to the other or a pair of mirrors in-between cube and objective. The issue with the mirrors is that the space between the lens and the Mitutoyo is at most of the order of 100 mm, given by the focal length of both. The phase difference between the beams can be adjusted by placing and tilting a phase plate in one of the beam paths. Here a clever scheme to place the central fringe to a precision of $\sim 1\mu\text{m}$ is still missing and needs test on atoms to finalize. Especially to see how well the alignment in front of the **NPBS** already allows to align the position of the central fringe.

In between the different optical components there is free space with the possibility and necessity for different components. For example position 1 in front of the **AOD** is the only space where no beamtranslation is taking place, therefore it is of advantage to place the lenses to adjust the waists and any other component which might lead to spherical aberrations there. For the $\lambda/2$ -waveplate needed to adjust the power splitting position 3 is of interest. In position 4 the **PBS** for cleaning the polarisation and a π -phase plate in case of blue detuning are situated. Additionally mirrors or a phase plate for the alignment are necessary.

Apart from the relevant components it might be nice to place a photodiode behind the mirrors to continuously check the power behind the **AOD** as well as other optics for example for imaging.

CONCLUSION AND OUTLOOK

In this thesis an overview over the [HQA](#) experiment was given including a discussion of the fundamental design choices, the current status of the experiment including the realisation of a 2D- and 3D-MOT and the setup and characterization of a first module, namely an accordion lattice to upgrade the [HQA](#) to be able to prepare two-dimensional systems in the future.

The first part of the thesis was about taking a step towards faster cycle times. The long term goal of the experiment is to have cycle times well below 1 s. One necessary step to realise this is to shorten the [MOT](#) loading from a few seconds to times on the order of 100ms. Key point to fast loading rates being the high powers in the laser beams. This thesis explained the path from setting up the laser system to the realisation of both [MOTs](#).

In summary a laser frequency lock to the existing spectroscopy, a laser distribution and the 2D/3D-MOT were realised. Passively stable doublepassmoduls were used to shift the frequencies of the spectroscopy, the cooler and repumper. With a beat note to a known laser the right frequencies were ensured. A free space distribution was built on the laser table before coupling the beams into fibers to use them on the experiment table for the [MOTs](#). The alignment of the [MOTs](#) and the pictures of the atom cloud were discussed in section 4.3. Recently the 3D-MOT was realized. Along the free viewports of the glass cell imaging of the atom cloud is possible. This will be used to optimize the atom number and loading rate. Turning knobs for optimisation are:

- the pushbeam, with respect to its power, alignment and detuning
- detunings of cooler and repumper
- strength of the magnetic field gradient
- fine alignment of the 2D-MOT

For the laser system over the last year no degrading of the laser power was noticeable. The implemented lock is at least stable for more than 2 weeks, longer has not been tested. With a beat note to a locked laser from a different laboratory the frequency fluctuation could be estimated to be less than 0.7MHz. This number includes the frequency fluctuation of both lasers. If needed, optimization can be done by investigating the bandwidth of the [MTS](#)-signal and delays along the signal.

The current laser is mainly used for the [MOTs](#), spectroscopy and distribution of spectroscopy light. All additional lasers at 671nm will in the future also use the SHG light as frequency reference. For imaging, a DLpro laser is intended to be used. A phase lock to the [TA-SHG](#) is envisaged here. This will be done via a beat note between both lasers as addressed in section 4.2.3. Preferably the beat note should be realized not in free space but fiber based to directly ensure a spacial and polarisation overlap. Here there are working solutions in this group that work stable and permit phase-locking at frequency differences from few MHz up to

10 GHz. Besides locking to a constant frequency offset, it also allows frequency jumps of a GHz within a $1 \mu\text{s}$ and frequency ramps with widely adjustable time sweeps.

The second part of the thesis shows the considerations taken towards building an accordion module. First tests of an accordion lattice mainly consisting of a [NPBS](#) were taken and a roadmap towards a module was created.

The accordion lattice presented in this thesis has a variable lattice spacing between $1 \mu\text{m}$ and $\sim 15 \mu\text{m}$. The upper limit of the lattice spacing depends on the chamfer cut and how close the beam separation can be driven without distortion. Effects of the chamfer cut can be seen in section [5.7.4](#). To minimize this in the future, the modular setup we will use a custom made [NPBS](#) cubes without chamfer cuts. The measurement of the phase stability showed central fringe movements during a ramp of the lattice spacing comparable to other setups but more than the depth of focus of the objective. It is still under investigation if the difference between linear stage and the [AOD](#) setup stem from the different cubes or from the alignment. Here tests with different cubes and a test setup with an aspherical lens after the [AOD](#) will yield clarification. Additionally the temporal stability of the system was investigated. The phase between the beams drifts over time and does not settle but on a very small scale. The drift over 5 days equals to drifts of an accordion lattice with active phase stabilisation. The most likely cause for this drift is slack of the components along the beam path. The passive stability of a module might be helpful here.

In section [5.8](#) the roadmap towards an accordion lattice module is portrayed. The different components needed for an accordion lattice, their placement and necessary DOFs are described. Before finalizing the module, tests of different cubes and the alignment on atoms need to be tested.

In particular, in the course of this thesis realizations of the underlying idea to make the experiment fast and modular were shown. While the accordion lattice module is not finalised, the approach of taking a [NPBS](#) and a high NA objective shows promising results and first steps towards a module were taken. Soon the loading rate of the [3D-MOT](#) will be known allowing to take the next steps towards faster cycle times.

Part III

APPENDIX

LIST OF FIGURES

Figure 1	BEC-BCS crossover	5
Figure 2	Conceptual ideas of HQA	6
Figure 3	Rendering of the vacuum setup.	8
Figure 4	Mounting of the vacuum chamber.	9
Figure 5	Interior of the TA-SHG	14
Figure 6	ECDL in Littrow configuration and gain profiles of an ECDL.	14
Figure 7	Autoalignment	16
Figure 8	Beam coming out of the TA-SHG	16
Figure 9	Power of TA-SHG	17
Figure 10	MTS Signal	18
Figure 11	Scheme of the lock set up configuration for the Red Pitaya.	20
Figure 12	Pulse measurement Lock	21
Figure 13	Scattering rate over detuning for different intensities	24
Figure 14	Optical molasses for $s_0 = 2$ and $\delta_0 = -\gamma$	24
Figure 15	Zeeman splitting, trap configuration	25
Figure 16	Energy levels of Lithium-6.	26
Figure 17	Locking scheme.	27
Figure 18	Doublepass	28
Figure 19	SHG setup	30
Figure 20	2D MOT chamber with 4 arms around the chamber.	31
Figure 21	Picture of the 2D-MOT.	33
Figure 22	Atom path from oven to 3D-MOT	33
Figure 23	Picture of the 3D-MOT.	34
Figure 24	1D spilling	37
Figure 25	Accordion lattice intersecting beam	38
Figure 26	Contrast equation	40
Figure 27	Simulation contrast	41
Figure 28	Simulation asymmetry	41
Figure 29	Accordion Raizen	43
Figure 30	Accordion Foot	44
Figure 31	Accordion Greiner	44
Figure 32	Misalignments cube	45
Figure 33	Transmission of the Mitutoyo objective	46
Figure 34	Beamtranslation AOD	46
Figure 35	Trapping frequencies 532 nm	48
Figure 36	Trapping frequencies 680 nm	49
Figure 37	Our Accordion lattice set-up	50
Figure 38	Mounting NPBS	51
Figure 39	Parallelism beams	52
Figure 40	Movements beams	52
Figure 41	Shift of beams in focal point	53
Figure 42	Picture of the lattice without PBS	54
Figure 43	Image of the lattice	55
Figure 44	Lattice spacing vs beam separation	56

Figure 45	Dynamic stability of the lattice.	57
Figure 46	Dynamic stability of the lattice.	57
Figure 47	Temporal stability of the lattice.	58
Figure 48	Close to chamfer.	59
Figure 49	Accordion module	60

ACRONYMS

AOD Acousto Optical Deflector. [43–50](#), [52](#), [55–57](#), [60](#), [61](#), [64](#)

AOM Acousto Optical Modulator. [16](#), [18](#), [27–30](#), [46](#), [50–52](#), [55](#), [57](#)

ECDL external-cavity diode laser. [13](#)

EOM Electro Optical Modulator. [18](#)

HQA Heidelberg Quantum Architecture. [2](#), [3](#), [6](#), [27](#), [37](#), [47](#), [63](#)

MOT Magneto Optical Trap. [3](#), [6](#), [7](#), [23](#), [27](#), [30–34](#), [63](#), [64](#), [67](#)

MTS modulation transfer spectroscopy. [18](#), [19](#), [63](#)

NPBS Nonpolarizing Beam Splitter. [3](#), [29](#), [44–47](#), [49–56](#), [58–61](#), [64](#)

PBS Polarizing Beam Splitter. [28](#), [29](#), [32](#), [43](#), [50](#), [53](#), [54](#), [61](#)

PDH Pound-Drever-Hall. [15](#), [16](#)

PID Proportional–Integral–Derivative Controller. [3](#), [18](#), [19](#), [21](#), [43](#), [44](#)

SHG Second Harmonic Generation. [14–16](#)

TA Tapered Amplifier. [13](#), [15–17](#)

TA-SHG Tapered Amplifier-Second Harmonic Generation. [13](#), [15](#), [63](#)

BIBLIOGRAPHY

- [1] N. D. Mermin and H. Wagner. "Absence of Ferromagnetism or Antiferromagnetism in One- or Two-Dimensional Isotropic Heisenberg Models." In: *Physical Review Letters* 17.22 (Nov. 28, 1966). Publisher: American Physical Society, pp. 1133–1136. DOI: [10.1103/PhysRevLett.17.1133](https://doi.org/10.1103/PhysRevLett.17.1133). URL: <https://link.aps.org/doi/10.1103/PhysRevLett.17.1133>.
- [2] P. C. Hohenberg. "Existence of Long-Range Order in One and Two Dimensions." In: *Physical Review* 158.2 (June 10, 1967). Publisher: American Physical Society, pp. 383–386. DOI: [10.1103/PhysRev.158.383](https://doi.org/10.1103/PhysRev.158.383). URL: <https://link.aps.org/doi/10.1103/PhysRev.158.383>.
- [3] N. D. Mermin. "Crystalline Order in Two Dimensions." In: *Phys. Rev.* 176 (1 Dec. 1968), pp. 250–254. DOI: [10.1103/PhysRev.176.250](https://doi.org/10.1103/PhysRev.176.250). URL: <https://link.aps.org/doi/10.1103/PhysRev.176.250>.
- [4] J. Toner. "Reanalysis of the hydrodynamic theory of fluid, polar-ordered flocks." In: *Physical Review E* 86.3 (Sept. 2012). DOI: [10.1103/PhysRevE.86.031918](https://doi.org/10.1103/PhysRevE.86.031918). URL: <https://doi.org/10.1103/PhysRevE.86.031918>.
- [5] Marvin Holten. *From Pauli Blocking to Cooper Pairs: Emergence in a Mesoscopic 2D Fermi Gas*. PhD thesis. 2022.
- [6] Micha Bunjes. *High-Resolution Optics for Modular Quantum Simulation*. Master thesis. 2022.
- [7] A. Bergschneider, V. M. Klinkhamer, J. H. Becher, R. Klemt, G. Zürn, P. M. Preiss, and S. Jochim. "Spin-resolved single-atom imaging of ${}^6\text{Li}$ in free space." In: *Phys. Rev. A* 97 (6 June 2018), p. 063613. DOI: [10.1103/PhysRevA.97.063613](https://doi.org/10.1103/PhysRevA.97.063613). URL: <https://link.aps.org/doi/10.1103/PhysRevA.97.063613>.
- [8] Ernst Ising. "Beitrag zur Theorie des Ferromagnetismus." In: *Zeitschrift für Physik* 31.1 (Feb. 1925), pp. 253–258. DOI: [10.1007/BF02980577](https://doi.org/10.1007/BF02980577).
- [9] L. Onsager. "Crystal Statistics. I. A Two-Dimensional Model with an Order-Disorder Transition." In: *Phys. Rev.* 65 (3-4 Feb. 1944), pp. 117–149. DOI: [10.1103/PhysRev.65.117](https://doi.org/10.1103/PhysRev.65.117). URL: <https://link.aps.org/doi/10.1103/PhysRev.65.117>.
- [10] Alan M. Ferrenberg, Jiahao Xu, and David P. Landau. "Pushing the limits of Monte Carlo simulations for the three-dimensional Ising model." In: *Physical Review E* 97.4 (Apr. 2018). DOI: [10.1103/PhysRevE.97.043301](https://doi.org/10.1103/PhysRevE.97.043301). URL: <https://doi.org/10.1103/PhysRevE.97.043301>.
- [11] R. C. Thompson-Flagg, M. J. B. Moura, and M. Marder. "Rippling of graphene." In: *EPL (Europhysics Letters)* 85.4 (Feb. 2009), p. 46002. DOI: [10.1209/0295-5075/85/46002](https://doi.org/10.1209/0295-5075/85/46002). URL: <https://doi.org/10.1209/0295-5075/85/46002>.
- [12] V. L. Berezinskiĭ. "Destruction of Long-range Order in One-dimensional and Two-dimensional Systems Possessing a Continuous Symmetry Group. II. Quantum Systems." In: *Soviet Journal of Experimental and Theoretical Physics* 34 (Jan. 1972), p. 610.

- [13] J. M. Kosterlitz and D. J. Thouless. "Ordering, metastability and phase transitions in two-dimensional systems." In: *Journal of Physics C: Solid State Physics* 6.7 (Apr. 1973), p. 1181. DOI: [10.1088/0022-3719/6/7/010](https://doi.org/10.1088/0022-3719/6/7/010). URL: <https://dx.doi.org/10.1088/0022-3719/6/7/010>.
- [14] P. Cladé, C. Ryu, A. Ramanathan, K. Helmerson, and W. Phillips. "Observation of a 2D Bose Gas: From Thermal to Quasicondensate to Superfluid." In: *Physical Review Letters* 102.17 (Apr. 2009). DOI: [10.1103/physrevlett.102.170401](https://doi.org/10.1103/physrevlett.102.170401). URL: <https://doi.org/10.1103/physrevlett.102.170401>.
- [15] W. Ketterle and M. W. Zwierlein. "Making, probing and understanding ultracold Fermi gases." In: *La Rivista del Nuovo Cimento* 31.506 (July 2008), pp. 247–422. ISSN: 0393697X, 0393697X. DOI: [10.1393/ncr/i2008-10033-1](https://doi.org/10.1393/ncr/i2008-10033-1). URL: <https://doi.org/10.1393/ncr/i2008-10033-1>.
- [16] Tobias Hammel. *Design and Construction of a New Experiment for Programmable Quantum Simulation using Ultracold ⁶Li Fermions*. Master thesis. 2021.
- [17] *Tunable Diode Lasers*. URL: <https://www.toptica.com/technology/technical-tutorials/tunable-diode-lasers>.
- [18] R. Paschotta. *Laser Diodes*. URL: <https://www.rp-photonics.com/laser-diodes.html> (visited on 10/20/2022).
- [19] Leo Walz. *Modulation Transfere Spectroscopy in Lithium-6*. Bachelor thesis. 2021.
- [20] Lennert Thormählen. *Implementation of a Versatile Digital Laser Lock for Imaging Ultracold Lithium*. Bachelor thesis. 2016.
- [21] T. Preuschoff, M. Schlosser, and G. Birkl. "Digital laser frequency and intensity stabilization based on the STEMlab platform (originally Red Pitaya)." In: *Review of Scientific Instruments* 91.8 (Aug. 2020), p. 083001. DOI: [10.1063/5.0009524](https://doi.org/10.1063/5.0009524). URL: <https://doi.org/10.1063/5.0009524>.
- [22] Martin Gerhard Ries. *A magneto-optical trap for the preparation of a three-component Fermi gas in an optical lattice*. Diploma thesis. 2010.
- [23] A. Ashkin and J. P. Gordon. "Stability of radiation-pressure particle traps: an optical Earnshaw theorem." In: *Opt. Lett.* 8.10 (Oct. 1983), pp. 511–513. DOI: [10.1364/OL.8.000511](https://doi.org/10.1364/OL.8.000511). URL: <https://opg.optica.org/ol/abstract.cfm?URI=ol-8-10-511>.
- [24] Michael E. Gehm. *Preparation of an optically-trapped degenerated Fermi gas of ⁶Li: Finding the route to degeneracy*. PhD thesis. 2003.
- [25] Marlene Matzke. *Design of a Compact Double Pass AOM Module*. Bachelor thesis. 2022.
- [26] T. G. Tiecke, S. D. Gensemer, A. Ludewig, and J. T. M. Walraven. "High-flux two-dimensional magneto-optical-trap source for cold lithium atoms." In: *Phys. Rev. A* 80 (1 July 2009), p. 013409. DOI: [10.1103/PhysRevA.80.013409](https://doi.org/10.1103/PhysRevA.80.013409). URL: <https://link.aps.org/doi/10.1103/PhysRevA.80.013409>.
- [27] Malaika Göritz. *Characterisation of a 2D-MOT for cooling ⁶Li*. Bachelor thesis. 2022.
- [28] T. C. Li, H. Kelkar, D. Medellin, and M. G. Raizen. "Real-time control of the periodicity of a standing wave: an optical accordion." In: *Optics Express* 16.8 (Apr. 2008), p. 5465. DOI: [10.1364/oe.16.005465](https://doi.org/10.1364/oe.16.005465). URL: <https://doi.org/10.1364/oe.16.005465>.

- [29] R. A. Williams, J. D. Pillet, S. Al-Assam, B. Fletcher, M. Shotter, and C. J. Foot. "Dynamic optical lattices: two-dimensional rotating and accordion lattices for ultracold atoms." In: *Optics Express* 16.21 (Oct. 2008), p. 16977. DOI: [10.1364/oe.16.016977](https://doi.org/10.1364/oe.16.016977). URL: <https://doi.org/10.1364%2Foe.16.016977>.
- [30] John Howard Huckans. *Optical Lattices and Quantum Degenerate ^{87}Rb in Reduced Dimensions*. PhD thesis. 2006.
- [31] Ram-Janik Petzold. *Few ultracold fermions in a two-dimensional trap*. Master thesis. 2020.
- [32] Anne Hebert. *A dipolar erbium quantum gas microscope. Doctoral dissertation, Harvard University Graduate School of Arts and Sciences*. PhD thesis. 2021.
- [33] Carolin Dietrich. *An accordion-type lattice: A tuneable dipole trap for ultracold gases*. Master thesis. 2018.
- [34] J. L. Ville et al. "Loading and compression of a single two-dimensional Bose gas in an optical accordion." In: *Physical Review A* 95.1 (Jan. 2017). DOI: [10.1103/physreva.95.013632](https://doi.org/10.1103/physreva.95.013632). URL: <https://doi.org/10.1103%2Fphysreva.95.013632>.
- [35] Sandra Brandstetter. *Towards the Creation of Vortices in a Dipolar Bose-Einstein Condensate*. Master thesis. 2020.
- [36] Lev Haldar Kendrick. *An Optical Accordion Trap for Two-Dimensional Ultracold Gases of ^6Li and ^{23}Na* . Bachelor thesis. 2019.
- [37] *Acousto-optic Theory Application Notes*. URL: <http://www.aaoptoelectronic.com/wp-content/uploads/documents/AAOPT0-Theory2013-4.pdf>.

ACKNOWLEDGMENT

Hello, old friend. And here we are. You and me, on the (nearly) last page. This journey would not have been possible without my family, my friends and many others.

First of all I would like to thank Selim for the supervision of this thesis and Lauriane for taking over the second examination. I want to thank the whole ultracold group, especially Tobi, Max and Micha for the great time. So long and thanks for all the laughter.

Last but not Laser, in hindsight of this thesis, I want to thank everybody involved in proofreading as well as everybody who has supported me along the way.

Erklärung:

Ich versichere, dass ich diese Arbeit selbstständig verfasst habe und keine anderen als die angegebenen Quellen und Hilfsmittel benutzt habe.

Heidelberg, den 01.01.23

.....